

ALI, O., AHMED, R., TOMA, F.-L., BERGER, L.-M., MATTHEY, B., FAISAL, N. and AHMED, K. [2023]. Influence of feedstock and thermal spray process on the phase composition of alumina coatings and their sliding wear. *Journal of thermal spray technology* [online], Online First. Available from: <https://doi.org/10.1007/s11666-023-01597-z>

# Influence of feedstock and thermal spray process on the phase composition of alumina coatings and their sliding wear.

ALI, O., AHMED, R., TOMA, F.-L., BERGER, L.-M., MATTHEY, B., FAISAL, N. and AHMED, K.

2023



# Influence of Feedstock and Thermal Spray Process on the Phase Composition of Alumina Coatings and Their Sliding Wear

Omar Ali<sup>1</sup> · Rehan Ahmed<sup>1</sup> · Filofteia-Laura Toma<sup>2</sup> · Lutz-Michael Berger<sup>3</sup> · Björn Matthey<sup>3</sup> · Nadimul Faisal<sup>4</sup> · Khalid Ahmed<sup>5</sup>

Submitted: 15 June 2022 / in revised form: 30 March 2023 / Accepted: 7 April 2023  
© The Author(s) 2023

**Abstract** Suspension thermal spraying is an emerging coating technology that enables the deposition of dense-structured ceramic coatings. As wear resistance is a main application field of alumina ( $\text{Al}_2\text{O}_3$ ) coatings, this study aimed to evaluate the dry reciprocating sliding wear resistance of suspension sprayed high velocity oxy-fuel (S-HVOF) alumina coatings and to compare it with atmospheric plasma sprayed (APS) and HVOF coatings. Coatings were analyzed in the as-sprayed state and post-treated at 910 °C (hot isostatically pressed, HIPed) conditions. Wear tests were conducted using a tribometer, following the ASTM G133-02 standard and a sintered WC-6 wt.% Co ball as the counterbody. Coating characterization was done using scanning electron microscopy, x-ray diffraction and nanoindentation technique. Results indicate that the HVOF, HVOF-HIP and S-HVOF coatings had a high  $\alpha$ - $\text{Al}_2\text{O}_3$  content, whereas the APS and APS-HIP coatings had a high  $\gamma$ -phase content together with high porosity. Sliding wear resistance was an order of magnitude higher for the S-HVOF and HVOF coatings than the APS and

APS-HIPed coatings. This difference in wear performance was attributed to the high nanohardness, elastic modulus, dense microstructure and relatively high  $\alpha$ - $\text{Al}_2\text{O}_3$  content in the HVOF, S-HVOF and HVOF-HIP coatings. Results are discussed in terms of the wear mechanism and structure-property relationship.

**Keywords** alumina coating · sliding wear · structure-property relationship · suspension · thermal spray coating · wear mechanism

## Introduction

As a sintered ceramic material, alumina ( $\text{Al}_2\text{O}_3$ ) is known for its extraordinary properties, such as a high melting point of 2054 °C, good mechanical and tribological properties, high chemical stability and high electrical resistance (Ref 1, 2). Abundance and relatively low costs are other reasons for the widespread use of alumina. Consequently, it is also a commonly used ceramic material for thermal spray coating solutions, where the main applications are electrical insulation and wear protection. Conventional atmospheric plasma spraying (APS) is the most important industrial spray process to manufacture these coatings (Ref 3-5). Other plasma spray processes are occasionally used, such as water stabilized plasma (WSP) spraying (Ref 4, 6-8). High velocity oxy-fuel spraying (HVOF) (Ref 9-11) and detonation gun spraying (DGS) (Ref 10, 12-15) produce coatings with lower porosity and higher bond strength. All these spray processes conventionally use feedstock powders to produce the coatings (Ref 9, 10). More recently, suspensions of finely dispersed alumina powders became an important feedstock both for APS and HVOF processes (Ref 9, 10, 16). Another important alumina feedstock is

✉ Rehan Ahmed  
R.Ahmed@hw.ac.uk

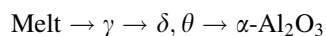
<sup>1</sup> School of Engineering and Physical Sciences, Heriot-Watt University, Edinburgh EH14 4AS, UK  
<sup>2</sup> Fraunhofer IWS, Fraunhofer Institute for Materials and Beam Technology, Winterbergstrasse 28, 01277 Dresden, Germany  
<sup>3</sup> Fraunhofer IKTS, Fraunhofer Institute for Ceramic Technologies and Systems, Winterbergstrasse 28, 01277 Dresden, Germany  
<sup>4</sup> School of Engineering, Robert Gordon University, Garthdee Road, Aberdeen AB10 7GJ, UK  
<sup>5</sup> College of Engineering, Alfaisal University, Riyadh 11533, Saudi Arabia

cords (Ref 17). With few exceptions in research (Ref 18, 19), all feedstock materials consist of the thermodynamically stable phase (corundum). Lower purity feedstocks may contain some  $\beta$ - $\text{Al}_2\text{O}_3$  ( $\text{NaAl}_{11}\text{O}_{17}$ ) due to a high sodium content as the main impurity, e.g., (Ref 20, 21).

Thermal spraying of alumina is strongly influenced by its polymorphism. Without special measures, the  $\alpha$ - $\text{Al}_2\text{O}_3$  existing in the feedstocks (both conventional feedstock powders and suspensions) transforms in all spray processes, predominantly to metastable crystalline phases and to an amorphous/nanostructured phase in the coating. It was initially described by Ault that flame-sprayed coatings from rods consist of  $\gamma$ - $\text{Al}_2\text{O}_3$  (Ref 22). Indeed, the absolute majority of references on coatings prepared by APS using conventional feedstock powders report the existence of predominately  $\gamma$ - $\text{Al}_2\text{O}_3$ , with some remaining  $\alpha$ - $\text{Al}_2\text{O}_3$  as crystalline phases, e.g., (Ref 3, 4, 23–30). The presence of  $\gamma$ - $\text{Al}_2\text{O}_3$  in the coating is due to the high cooling rate and nucleation of the undercooled melt (Ref 4, 23). The presence of the remaining  $\alpha$ - $\text{Al}_2\text{O}_3$  in the coating has been explained by the occurrence of unmelted particle cores (Ref 3, 4, 23, 30), or often just as unmelted particles. A systematic change of the APS process parameters, like primary and secondary gas flow rates, spray distance and nozzle diameter, has shown the corresponding dependencies (Ref 24). It was also shown that  $\delta$ - $\text{Al}_2\text{O}_3$  appears in as-sprayed APS coatings on copper substrates, and that its content depends on the spray distance (Ref 31). By using APS and sintered alumina substrates, it has been observed that the substrate temperature is decisive for the formation of an amorphous phase,  $\gamma$ - $\text{Al}_2\text{O}_3$  or  $\alpha$ - $\text{Al}_2\text{O}_3$  (Ref 32).

In addition to the explanation on the appearance of  $\gamma$ - $\text{Al}_2\text{O}_3$  in the coating given by McPherson et al. (Ref 3, 23), it is proposed that  $\text{Al}_2\text{O}_3$  undergoes a structural rearrangement from an octahedral to a tetrahedral coordination on melting, making in the case of quenching the crystallization of tetrahedral crystalline phases like  $\gamma$ - $\text{Al}_2\text{O}_3$  more probable (Ref 33). This phase transformation deteriorates the corrosion, e.g., (Ref 34), and the electrical insulation properties, e.g., (Ref 15, 20).

A detailed review of transition sequences of metastable alumina polymorphs (Ref 33) states that after the formation of a melt, the following sequence back to  $\alpha$ - $\text{Al}_2\text{O}_3$  is observed:



A high-temperature treatment or service temperature at  $\geq 900$  °C leads to changes in the phase composition, ending with a full transformation from  $\gamma$ - $\text{Al}_2\text{O}_3$  to  $\alpha$ - $\text{Al}_2\text{O}_3$  at about 1180 °C (with sufficient heat treatment time). This transformation is important, as due to the density differences between the  $\gamma$ - $\text{Al}_2\text{O}_3$  (3.65–3.67 g/cm<sup>3</sup> (Ref 33)) and

$\alpha$ - $\text{Al}_2\text{O}_3$  (3.99 g/cm<sup>3</sup> (33)), the formation of defects, in particular cracks, is common in coatings (Ref 4, 21, 25). This transformation has been studied for APS (Ref 21, 35, 36) and suspension high velocity oxy-fuel (S-HVOF) (Ref 37) coatings, but still in more detail for small bulks manufactured by WSP (Ref 38). For APS and WSP coatings,  $\delta$ - $\text{Al}_2\text{O}_3$  was observed at 900 °C (Ref 35, 36, 38), while  $\theta$ - $\text{Al}_2\text{O}_3$  was found at higher temperatures. However, Damani and Makroczy (Ref 38) have shown that the full transformation to  $\alpha$ - $\text{Al}_2\text{O}_3$  depends both on temperature and time. Thus, the transition phases can appear at different temperatures. Occasionally, additional differing modifications of the  $\delta$ - $\text{Al}_2\text{O}_3$  instead of the  $\theta$ - $\text{Al}_2\text{O}_3$  were observed, e.g., for an APS coating (Ref 21) and S-HVOF coatings (Ref 37). Detailed structural discussions have revealed that  $\gamma$ - $\text{Al}_2\text{O}_3$  has a defective spinel-like structure, while for  $\delta$ - $\text{Al}_2\text{O}_3$  different structural variants exist (Ref 39–41). However, the crystallographic structure of  $\delta$ - $\text{Al}_2\text{O}_3$  is contradictorily discussed in the literature (Ref 33, 39–41). Differences in the  $\gamma$ - $\text{Al}_2\text{O}_3$  defect structure can result in different variants of  $\delta$ - $\text{Al}_2\text{O}_3$  (Ref 39), but it can also be bypassed, and  $\theta$ - $\text{Al}_2\text{O}_3$  is formed directly from  $\gamma$ - $\text{Al}_2\text{O}_3$  (Ref 41).

In addition, detailed investigations on coating formation described in the literature have shown that the content of the amorphous phase, as well as  $\alpha$ - $\text{Al}_2\text{O}_3$  and  $\gamma$ - $\text{Al}_2\text{O}_3$ , can be locally different in the coating. In particular, the faster cooling rate for the first layer leads to amorphous phase formation (Ref 26, 42). As the increase of  $\alpha$ - $\text{Al}_2\text{O}_3$  content in the coating is expected to significantly improve the coating properties, many efforts have been made to reach this objective. The amount of  $\alpha$ - $\text{Al}_2\text{O}_3$  can be increased by selecting special spray process conditions (Ref 4, 21, 32, 43, 44), but these approaches are not suitable to be introduced into industrial practice. It has also been shown that heating the substrates up to 660 °C does not significantly increase the  $\alpha$ - $\text{Al}_2\text{O}_3$  content (Ref 45). Thus, the use of suspensions (Ref 10, 16, 46, 47) and solutions (Ref 43, 44) appears most promising. Another way is to stabilize  $\alpha$ - $\text{Al}_2\text{O}_3$  by  $\text{Cr}_2\text{O}_3$ , which is also widely discussed in the literature (Ref 4, 6, 7), most recently also by additional blending with  $\text{TiO}_2$  (Ref 48) or alloying of  $\text{Al}_2\text{O}_3$  - with  $\text{TiO}_2$  only (Ref 49).

The spray process significantly influences the wear resistance of alumina coatings. Due to the lower porosity and improved mechanical properties, HVOF coatings show an improved sliding wear resistance, e.g., (Ref 5, 9, 10, 50). However, the fracture toughness and ductility of oxide coatings are low compared to wear resistant hardmetal coatings such as WC-Co (Ref 51–54). The sliding wear resistance of thermal spray coatings depends on the coating microstructure, mechanical strength, residual stress and tribological test conditions. Previously, the authors

analyzed the sliding wear resistance of conventional thermally sprayed alumina coatings, where the dependency of microstructural phases on the wear performance was discussed (Ref 5).

Table 1 summarizes the literature investigating the sliding wear resistance of plain alumina (including grades with impurities but without alloying elements), coatings to compare their tribological performance (Ref 18, 29, 37, 45, 47, 55–68). Wear rate, test methodology and mechanical properties such as hardness and fracture toughness, where available in the literature, are included in Table 1. As can be seen, alumina coatings' wear rate can vary by orders of magnitude depending upon the coating microstructure and tribological test conditions. While studies related to the sliding wear resistance have been frequently reported, investigations related to the comparison of suspension-sprayed coatings with conventional alumina coatings are limited (Ref 37, 69).

This contribution aims to compare the sliding wear resistance of suspension sprayed high velocity oxy-fuel (S-HVOF) alumina coatings against sintered WC-Co counterbodies. This selection was based on previous studies, showing that the suspension spraying allows to produce dense and nanostructured alumina coatings with higher content  $\alpha$ -Al<sub>2</sub>O<sub>3</sub> content (Ref 5, 16, 70, 71). The S-HVOF coating was compared with conventional APS and HVOF coatings. After spraying, the coatings were post-treated using the hot isostatic pressing (HIPing) process. The coatings in the as-sprayed and post-treated conditions were characterized by SEM and XRD. The influence of the relationship between the spray process, feedstock and coating properties is discussed.

## Experimental

### Spray Processes and Post-Treatment

Alumina coatings were deposited using APS, HVOF and S-HVOF spraying techniques starting from different spray feedstocks, as summarized in Table 2. The powder morphologies are shown in Fig. 1. HVOF and APS coatings were acquired from a commercial source (Fujimi Inc., Japan) (Ref 52). Details of the substrate's thermal history during deposition and the deposition efficiency are not known due to commercial sensitivity. As reported previously, APS and HVOF feedstock powders consisted of  $\alpha$ -Al<sub>2</sub>O<sub>3</sub> (Ref 52), whereas the APS process is commercially widely used, a particular HVOF process ( $\theta$ -gun, WHITCO, Japan), based on special features of the spray gun construction (Ref 72–74) and using fine alumina powder, was applied in this study. For S-HVOF spraying, a water-based suspension containing fine  $\alpha$ -Al<sub>2</sub>O<sub>3</sub> powder was used as

feedstock. The S-HVOF coating was produced at Fraunhofer IWS using a modified HVOF TopGun (GTV Verschleißschutz GmbH, Germany) and an appropriate pressurized suspension feeder, as described previously (Ref 16). APS and HVOF coatings were deposited on AISI 440C steel disks of diameter 31 mm and thickness 8 mm. S-HVOF coatings were deposited on square plates of sides 30 mm and thickness 3 mm on a low carbon steel substrate. The substrates were sand-blasted with corundum prior to spraying. A post-treatment of these coatings was performed in argon environment using hot isostatic pressing (HIPing) at a temperature and pressure of 910 °C and 103.2 MPa, respectively, for 2 h in unencapsulated conditions. The heating and cooling rates were low in the range of 8.7–9.0 °C min<sup>-1</sup> and 5.8–6.9 °C min<sup>-1</sup>, respectively, to avoid cracking in the coating. HIPing post-treatment was conducted to promote intersplat bonding and phase transformation with a view to improve tribo-mechanical performance of coatings. Although during HIPing a full transformation to  $\alpha$ -Al<sub>2</sub>O<sub>3</sub> was not expected at this temperature, this HIPing temperature was chosen because of the substrate material's considerations.

### Coating Characterization

Coatings were characterized using scanning electron microscopy (SEM) including energy-dispersive x-ray spectrometry (EDS), x-ray diffraction (XRD), Vickers microhardness, and nanoindentation techniques. Cold mounted specimens were used after cutting to prepare coating cross sections by metallographic techniques. XRD analysis was performed using an ID3003 TT (GE Sensing and Inspection Technologies, GmbH) x-ray diffractometer operating at 40 kV and 30 mA, using Cu-K $\alpha$  radiation (wavelength  $\lambda = 0.1542$  nm) in the  $2\theta$ -region of 5–90° and a step size of 0.03°. A semi-quantitative analysis of the crystalline phases was performed by a Rietveld refinement using the software TOPAS V6 (Bruker AXS, USA) and structural data of the ICSD ( $\alpha$ -Al<sub>2</sub>O<sub>3</sub>(R-3c),  $\beta$ -Al<sub>2</sub>O<sub>3</sub>(P63/mmc),  $\alpha$ -Al<sub>2</sub>O<sub>3</sub>(I41/and, Fd-3m) and  $\beta$ -Al<sub>2</sub>O<sub>3</sub> (C2/m)) as well as the Pearson ( $\gamma$ -Al<sub>2</sub>O<sub>3</sub>(P212121)) database. A fully quantitative analysis using an external standard, and as applied by Bolelli et al. (Ref 37), was not possible to perform in the framework of this study. Coating porosity was determined by image analysis using ImageJ software in accordance with the ASTM E2109 standard. Vickers microhardness HV0.2 at a load of 1.96 N was measured using a calibrated MVK-H1 (Mitutoyo, Japan) device. At least five measurements were made on each polished coating top-surface. Nano-hardness and elastic modulus measurements were performed using a calibrated nanoindentation system (NanoTest<sup>TM</sup>-Micro Materials Limited, UK) equipped with a standard Berkovich nanoindenter tip. Measurements on

**Table 1** Comparison of wear rates for alumina coatings from published literature

Coating material	Material trade name	Spray method	Hardness	Fracture toughness (MPa·m <sup>1/2</sup> )	Wear conditions	Counter body	Friction coefficient	Coating wear rate (× 10 <sup>-6</sup> mm <sup>3</sup> /N·m)	Phases in coating	Reference (year)
Al <sub>2</sub> O <sub>3</sub> suspension:	GTV suspension	S-HVOF, Top Gun, GTV			Ball on flat	Al <sub>2</sub> O <sub>3</sub> ball	–		γ / α	[18]
(a) as-sprayed			9 ± 1 GPa	~ 0.8 ± 0.1	L = 16.8 N			0.0055		[18]
(b) Heat-treated at 600 °C, 6 h			12 ± 2 GPa	0.7 ± 0.1	V = 20 mm/s			0.0029		(2019)
(c) Heat-treated at 750 °C-6 h			14 ± 3 GPa	~1.2 ± 0.2	D = 36 m			~ 0.1		
(d) Heat-treated at 750 °C-48 h			16 ± 3 GPa	~ 1.7 ± 0.5	Reciprocating			~ 1		
Al <sub>2</sub> O <sub>3</sub>	6060 Amdry, Sulzer Metco	APS	820–1150	–	Pin on Disc L = 50, 100, 160 N V = 1.4 m/s	D2 tool steel (60HRC)	0.45 ... 0.55	5000 ... 2500	Main γ-phase	[29] (2000)
Al <sub>2</sub> O <sub>3</sub>	MRS2, Martinswerk	HVSFS	1000 ... 1200	–	Rotary	Al <sub>2</sub> O <sub>3</sub> ball	0.61 ... 0.67	~0.62 ... 1.31	γ: 46.9–84.6% α: 1–8% Glassy: 13.6 - 45.1%	[37] (2015)
D50 = 1.26 μm	APA-0.5, Sasol, Tucson				Ball on disc L = 10 N V = 0.1 m/s D = 1000 m Track radius = 5 mm					
D50 = 0.55 μm					Rotary					
Al <sub>2</sub> O <sub>3</sub>	AuerCoat suspension, Treibacher	SPS, KK Gun, AMT	672 ... 1004	–	Ball on disc L = 10 N	Al <sub>2</sub> O <sub>3</sub> ball	~0.66 ... 0.7	8.47 ... 47	γ: 38–67%	[47] (2020)
	MARTOXID MZS-1, Martinswerk	S-HVOF, Top-Gun, GTV			V = 0.1 m/s D = 1000 m Track radius = 8 mm				γ: 36–62%	
					Rotary					
Al <sub>2</sub> O <sub>3</sub>	Conventional-Praxair	APS, F4 Gun,	~8 ... 9.5 GPa	~1.3	Ball on disc (ASTM G99-17) L = 5, 10 N V = 0.2 m/s	SiC	~0.6 ... 0.85	Below 1 in all cases at room temperature tests	α: 5.1%	[50] (2007)
HVOF-Conventional	Nanostructured powder	HVOF, HV-2000 Gun Praxair	~9 ... 10 GPa	~2.4	D = 500 m Track radius = 8 mm				α: 9.2%	
HVOF-Nanostructured			~9 ... 10 GPa	~2.5	Rotary				α: 5.2%	
Al <sub>2</sub> O <sub>3</sub> -40 wt% aqueous suspension,	Treibacher	SPS (122 kW)	998	–	Ball on disc L = 10N	Al <sub>2</sub> O <sub>3</sub> ball	0.61	0.04	–	[55] (2017)
Al <sub>2</sub> O <sub>3</sub> spray powder	Amperit 740 (H.C. Starck)	Mettech Axial III APS (124 kW)	1361		V = 0.1 m/s D = 157 m Track radius = 5 mm		0.75	0.55		
					Rotary					

**Table 1** continued

Coating material	Material trade name	Spray method	Hardness	Fracture toughness (MPa·m <sup>1/2</sup> )	Wear conditions	Counter body	Friction coefficient	Coating wear rate (× 10 <sup>-6</sup> mm <sup>3</sup> /N·m)	Phases in coating	Reference (year)	
Al <sub>2</sub> O <sub>3</sub> suspension	31Tt40	SPS-WSP-H500 (~150 kW)	-	-	Pin on Disc L = 10 N V = 0.1 m/s D = 2000 m	-	-	2.38 ± 1.06	α: 25 wt%	[56]	
	25E10							0.194 ± 0.053	α: 10 wt%	(2017)	
	AW24							2.03 ± 0.07	α: 10 wt%		
Al <sub>2</sub> O <sub>3</sub>	Suspension	S-HVOF at: (a) 101 kW (b) 101 kW (c) 72 kW	HV 200 gf 1326 1326 1173	~ 1 ~ 3.5	Rotary Ball on flat L = 10 N V:0.01 m/s Stroke = 5 mm Reciprocating Pin on disc L = 2 N V = 0.05 m/s D = 800 m	Al <sub>2</sub> O <sub>3</sub> ball	-	~ 40 to 40	-	[57]	
								~ 0.2 to 0.4		(2016)	
								295 ...430		[58]	
										(2015)	
Al <sub>2</sub> O <sub>3</sub> 0 ... 15%	-	HVOF	-	-	Steel 68HRC	-	-				
Al <sub>2</sub> O <sub>3</sub>	a&s powder	APS (a) 450 A (b) 550 A (c) 625 A	Knoop 50 gf ~ 1200 ~ 1480 ~ 2150	-	Ball on flat L = 2 N Freq = 1 Hz Stroke = 15 mm D = 378 m	Al <sub>2</sub> O <sub>3</sub> ball	-	1259	γ-phase mainly present in 625 A coating	[59]	
								509			(2014)
								315			
Al <sub>2</sub> O <sub>3</sub>	50 vol.% below 500 nm	DGS (a) Low fuel (b) Medium fuel (c) High fuel	HV 200 gf 885 ... 993 832 ...1136 934 ... 1322	-	Ball on flat L = 10 N V = 0.005 m/s Stroke = 2 mm D = 400 m	Al <sub>2</sub> O <sub>3</sub> ball	-	0.6... 1.0	α-phase % 6.1...13.4 8.9...10.8 8.1...14.8	[60]	
								0.11...0.24			(2014)
								0.10...0.17			
Al <sub>2</sub> O <sub>3</sub> 80 nm	Agglom. Zibo Xinfumeng	APS 3 MB	200 gf HV 1152.5 960	-	Reciprocating Pin on disc L = 30 ... 80 N	Steel EN32	-	0.90 ...0.85	α-phase	[61]	
								3.10 ...7.05			(2011)
								4.60 ...9.21			
Al <sub>2</sub> O <sub>3</sub> 40 μm	Fine Chemicals Ltd, Mumbai	SPS, F4 Gun,	-	-	Pin on disc L = 2 N V = 0.1 m/s D = 1500 m	Al <sub>2</sub> O <sub>3</sub> ball	-	0.0052...0.0037	δ-phase	[62]	
								0.39...0.044			(2010)
Al <sub>2</sub> O <sub>3</sub>	P512 SB, Alcan	-	-	-	Rotary	-	-				

Table 1 continued

Coating material	Material trade name	Spray method	Hardness	Fracture toughness (MPa·m <sup>1/2</sup> )	Wear conditions	Counter body	Friction coefficient	Coating wear rate (× 10 <sup>-6</sup> mm <sup>3</sup> /N·m)	Phases in coating	Reference (year)
Al <sub>2</sub> O <sub>3</sub>	P172SB AKP30	SPS	-	-	Ball on disc L = 2 N V = 0.1 m/s D = 1500 m Rotary	Al <sub>2</sub> O <sub>3</sub> ball	~0.2... 0.5	~0.08...0.99	α and γ	[63] (2009)
Al <sub>2</sub> O <sub>3</sub>	Nano Conv Conv	HVSFS APS HVOF	1122 917 765	-	Pin on disc L = 5 N D = 500 m Rotary	Al <sub>2</sub> O <sub>3</sub> ball	-	~24.0 ~300 ~410	α/γ ratio 2.8 7.5 22.8	[64] (2009)
Al <sub>2</sub> O <sub>3</sub>	Medicoat-f&c P512SB-Alcan	APS SPS	-	-	Ball on disc L = 2 N V = 0.1 m/s D = 1500 m Rotary	Al <sub>2</sub> O <sub>3</sub> ball	~0.9 ~0.4 to 0.5	Wear depth ~19 μm ~3 μm	-	[65] (2008)
Al <sub>2</sub> O <sub>3</sub> - conventional	HVOF	-	HV 1N ~ 10 GPa ~ 9.3 GPa	~ 2.3 ... 2.5 ~ 1.15	Ball on disc L = 10 N V = 0.2 m/s D = 500 m Rotary	SiC	-	~ 0.81	α-phase % 9.2	[66] (2008)
Al <sub>2</sub> O <sub>3</sub> -nano	APS	-	-	-	Pin on disc L = = 5 N V = 0.2 m/s D = 250 m Rotary	Al <sub>2</sub> O <sub>3</sub> ball	~ 0.87	1120...1330	-	[67] (2006)
Al <sub>2</sub> O <sub>3</sub> - conventional	APS	APS F4	IN HV 11.7 ± 1.7	2.57 ± 0.65	Pin on disc L = = 5 N V = 0.2 m/s D = 250 m Rotary	Al <sub>2</sub> O <sub>3</sub> ball	~ 0.8 ~ 0.6	1000 250	α-phase 3% 7%	[68] (2001)

(SPS: suspension plasma spraying; slph: standard liters per hour; SD: spray distance; DGS: detonation gun spraying; APS: atmospheric plasma spraying; HVOF: high velocity oxy-fuel spraying; S-HVOF / HVSFS: suspension high velocity oxy-fuel spraying; L = normal load; V = sliding velocity; D = sliding distance)

**Table 2** Thermal spray parameters (Ref 20, 25)

Spray Gun	Feedstock and spray conditions	
9-MB (APS)	Spray material	Angular/crushed alumina ( $\text{Al}_2\text{O}_3 > 98.0\%$ )
	Powder size distribution	10-45 $\mu\text{m}$
	Arc current	500 A
	Arc voltage	70 V
	Primary gas, Ar	37.6 L/min
	Secondary gas, H <sub>2</sub>	7.1 L/min
	Spray distance	80 mm
θ-Gun (HVOF)	Spray material	Angular/crushed powder alumina ( $\text{Al}_2\text{O}_3 > 98.0\%$ )
	Powder size distribution	1-5 $\mu\text{m}$
	Oxygen flow rate	893 L/min
	Kerosene flow rate	0.3 L/min
	Acetylene flow rate	43 L/min
	Spray distance	150 mm
Modified Top Gun (S-HVOF)	Spray material	Aqueous suspension of fine raw powder alumina ( $\text{Al}_2\text{O}_3 > 99.9\%$ ), 35 wt.% solid content of $\text{Al}_2\text{O}_3$
	Particle size distribution	0.4-3.5 $\mu\text{m}$
	Oxygen flow rate	230 L/min
	Ethylene flow rate	75 L/min
	Spray distance	80 mm

coating-substrate cross sections were performed at room temperature ( $\sim 23\text{ }^\circ\text{C}$ ) in load control mode at a load of 100 mN. Indentation hardness and modulus results were based on the real-time load-displacement curve and were analyzed using the Oliver and Pharr method (Ref 75).

### Sliding Wear Investigation

The dry sliding wear resistance of coatings was investigated using a ball-on-disk reciprocating sliding wear tribometer (BLR2000 M, Bud Labs, USA) at room temperature in accordance with the ASTM G133-02 standard. Sliding wear test and counterbody details are listed in Table 3. Wear tests were repeated five times for each coating. Coating volume loss was measured using an interferometer (Zygo New View, USA). Wear track cross sections were measured at three points and averaged value was used in the volume loss calculation. Ball volume loss was calculated using its mass loss measured with a weighing scale of accuracy  $10^{-5}$  g. Friction force was measured using a tension-compression load cell mounted on the testing equipment. Wear tracks were analyzed using a SEM in Secondary Electron (SE) and Back Scattered Electron (BSE) mode along with the elemental mapping (EDS) to study the wear mechanisms.

## Results

### Coating Microstructure and Hardness

To reveal the lamella microstructure of the coatings, they were cooled in liquid nitrogen and fractured to visualize the intersplat morphology. Figure 2 provides the cross sections of the fractured APS, HVOF and S-HVOF coatings. The APS and HVOF coatings show distinct intersplat boundaries, whereas the S-HVOF coating shows a much finer nodular structure (Fig. 2d). Figure 3 shows the polished cross-sectional micrographs of the as-sprayed and HIPed coatings. There was evidence of crack formation within the coating microstructure due to thermal stresses and particle sintering after HIPing. Surface cracks were observed in all HIPed coatings, and subsequent grinding and polishing of samples was conducted, which resulted in their lower thickness than their as-sprayed counterparts. The extent of grinding and polishing required for the APS-HIP coating was extensive, resulting in a significant reduction in coating thickness. Some vertical cracks were visible in the HVOF coating after HIPing, as shown in Fig. 3(d). The S-HVOF coating showed intensive microcracking after HIPing, as shown in Fig. 3(f), leading to partial delamination of coating segments between cracks. Higher magnification SEM observations of coatings are shown in Fig. 4.

Averaged porosity values of the as-sprayed and HIPed coatings are summarized in Fig. 5. The average porosity



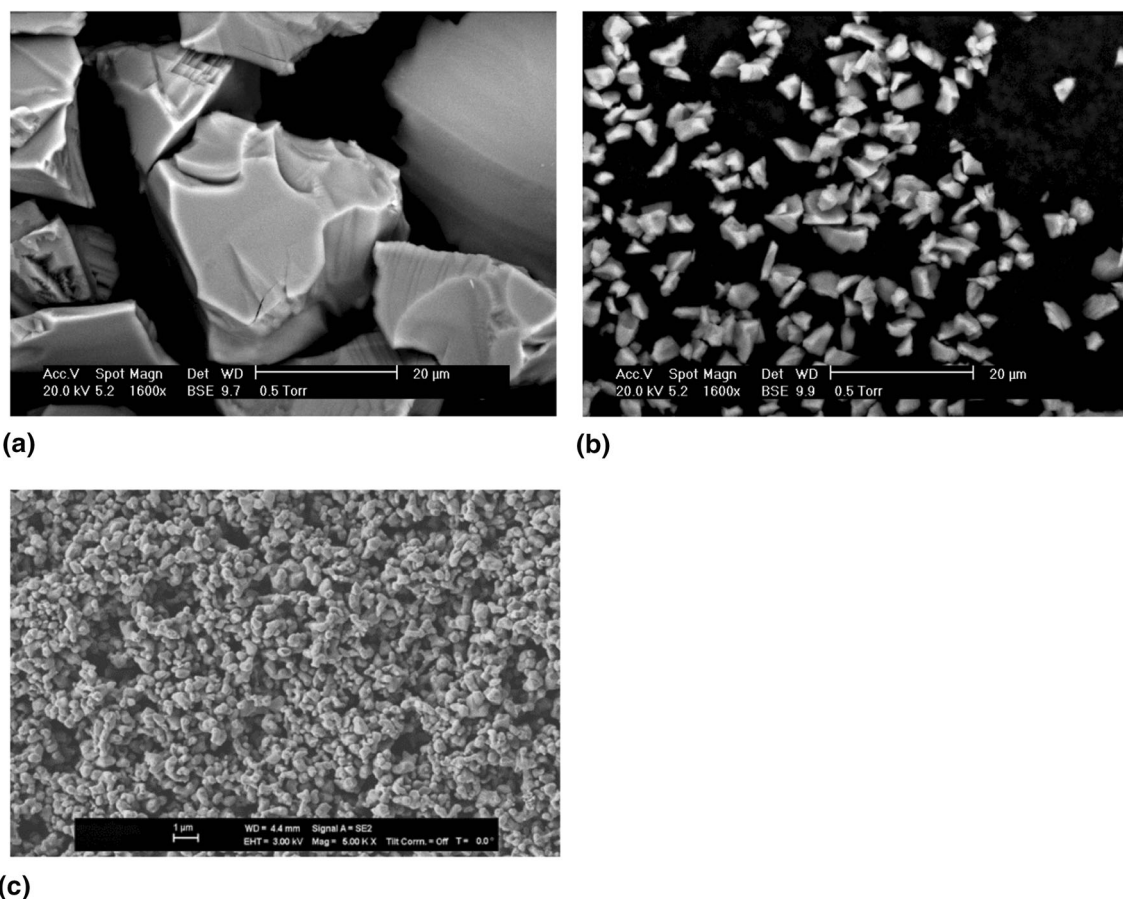


**Fig. 1**  $\text{Al}_2\text{O}_3$  feedstock powders and their particle size range (a) APS: 10–45  $\mu\text{m}$  (b) HVOF: 1–5  $\mu\text{m}$  (c) S-HVOF: 0.4–3.5  $\mu\text{m}$

**Table 3** Sliding wear test parameters

Normal load, N	25
Stroke length, mm	10
Sliding distance, m	500
Frequency, Hz	2
Counterbody material	sintered WC-6 wt.% Co
Counterbody ball diameter	9.53 mm (3/8 inch)
Density of WC-Co ball (manufacturers data)	14.95 $\text{g}/\text{cm}^3$
Ultimate tensile strength of WC-Co ball (manufacturer data)	1.516 GPa
Hardness of WC-Co ball (manufacturer data)	Rockwell 'A' 90.5–91.5

values for the HIPed coatings represent measurements in areas without cracks. Figure 6 shows the XRD analysis of the as-sprayed and HIPed coatings. The results of the semi-quantitative analysis of the crystalline phases are compiled in Table 4. Figure 7 shows the through-thickness hardness and elastic-modulus results for the coatings in the as-sprayed and HIPed conditions. The HIPed coatings cracked, and hence only representative values in the crack free zone are represented. The Vickers microhardness values indicate values of  $683 \pm 38$  HV0.2,  $632 \pm 29$  HV0.2 and  $851 \pm 115$  HV0.2, for the APS, HVOF and S-HVOF coatings, respectively.

### Sliding Wear Test

The averaged coefficient of friction (CoF) values derived from the five tests for each couple are plotted against sliding distance along with their respective standard deviation in Fig. 8(a, b). The wear rate of the as-sprayed and HIPed coatings in terms of coating wear, ball wear and total wear of the test couples is shown in Fig. 8(c). A summary of the ball, coating and total wear losses of the test couples is shown in Table 5. The average CoF for the steady-state, calculated from the last 300 m of the wear tests is also shown in the same Figure (Fig. 8a, b).

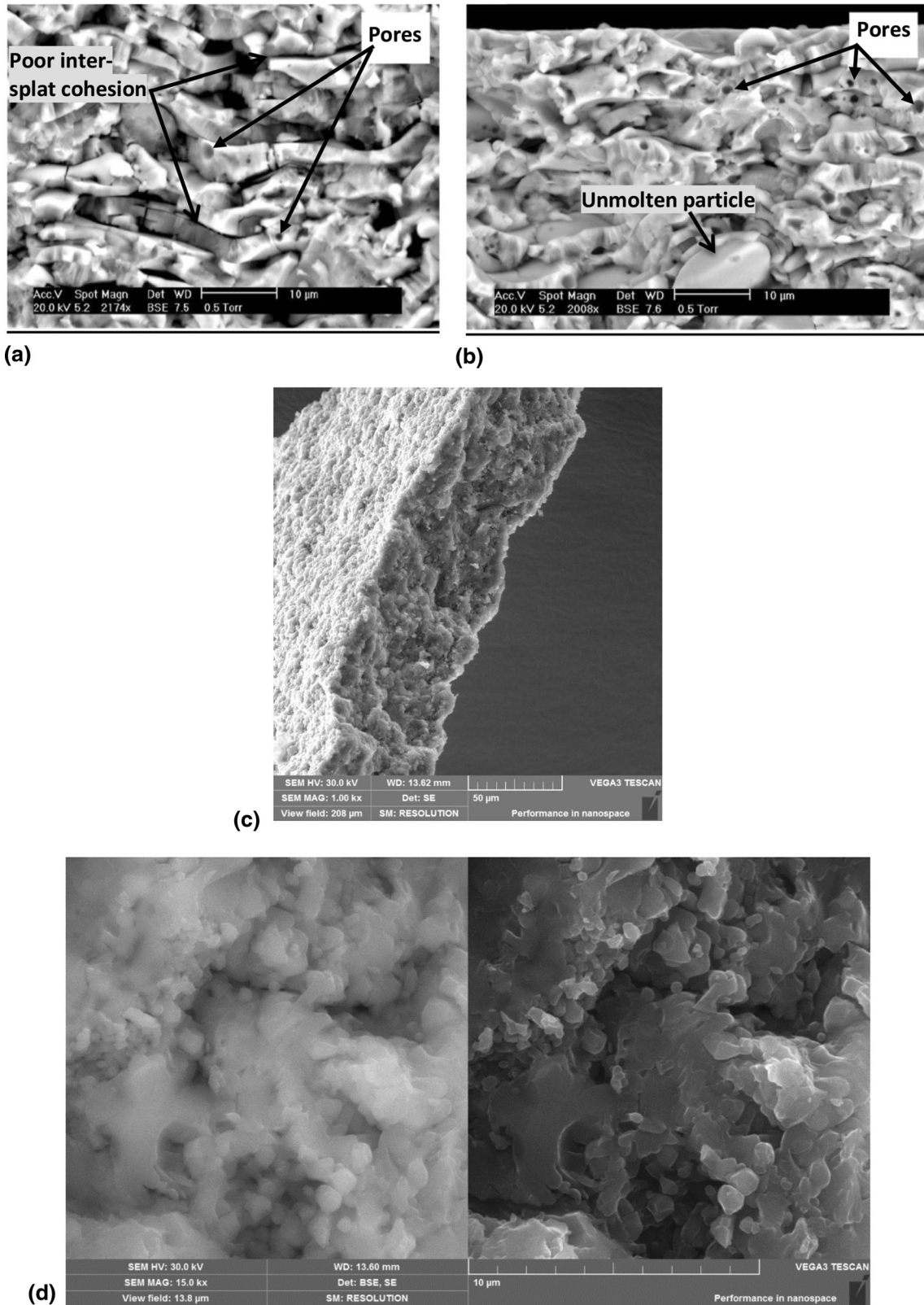


**Fig. 2** Fractured cross-sectional SEM micrographs of (a) APS (Ref 52), (b) HVOF (Ref 52), (c) S-HVOF low magnification, and (d) S-HVOF high magnification (BSE and SE mode, respectively). (a) and (b) reprinted from R. Ahmed, N. H. Faisal, A. M. Paradowska,

and M. E. Fitzpatrick, Residual strain and fracture response of  $Al_2O_3$  coatings deposited via APS and HVOF techniques, *Journal of Thermal Spray Technology*, Vol. 21, pg. 23-40, 2012, Springer Nature

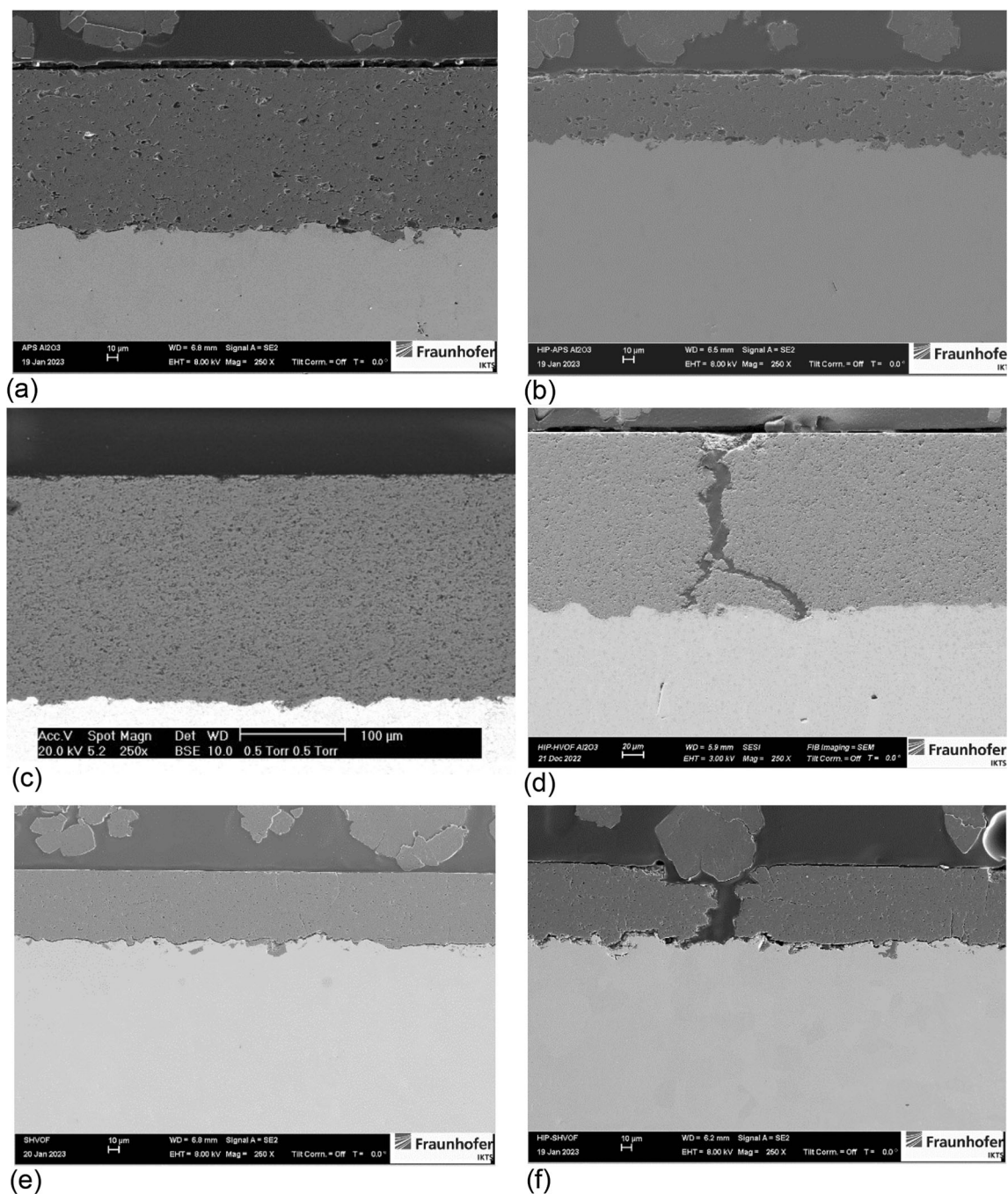


**Fig. 3** Polished low magnification cross-sectional SEM micrographs of coatings, as-sprayed and after HIPing post treatment (a) APS, (b) APS-HIP, (c) HVOF, (d) HVOF-HIP, (e) S-HVOF and (f) S-HVOF-HIP

SEM images of the wear scars for the as-sprayed and HIPed coatings are presented in Fig. 9. The EDS map and the spectrum data are also given for the wear scars. Because of significant coating segment delamination due to crack formation, the wear volume loss analysis on the S-HVOF-HIPed coatings could not be accurately performed after the sliding wear tests. These results are

therefore not included in Fig. 8. Macrocracking in the HIPed HVOF coating could be observed (Fig. 9e(i)). However, the coating did not delaminate, and the wear data are presented in Fig. 8. The macrocracking observed in Fig. 9e(i) was similar to a previously reported study of heat-treated alumina coatings (Ref 18). Figure 10 shows the typical wear debris morphology for the APS and HVOF

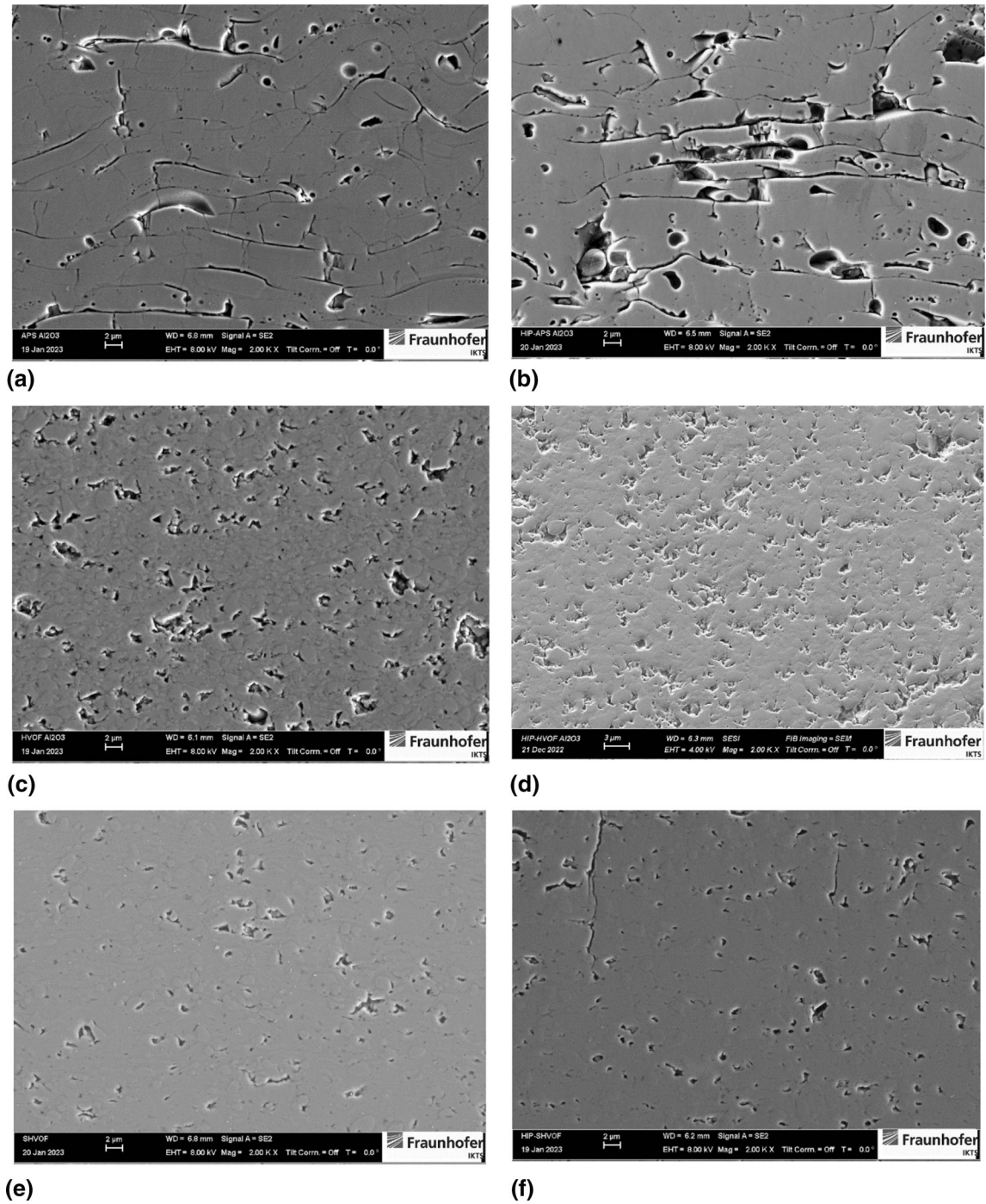


**Fig. 4** Polished cross-sectional SEM micrographs of coatings (a) APS, (b) APS-HIP, (c) HVOF, (d) HVOF-HIP, (e) S-HVOF and (f) S-HVOF-HIP

coatings. The debris for the S-HVOF coating was very fine and dispersed during the test and hence contaminated, hence not reported in Fig. 10. Figure 11 shows typical ball

wear at two different magnifications. Figure 12 provides a comparison of the wear track profiles in terms of their width and depth for the as-sprayed and HIPed coatings.

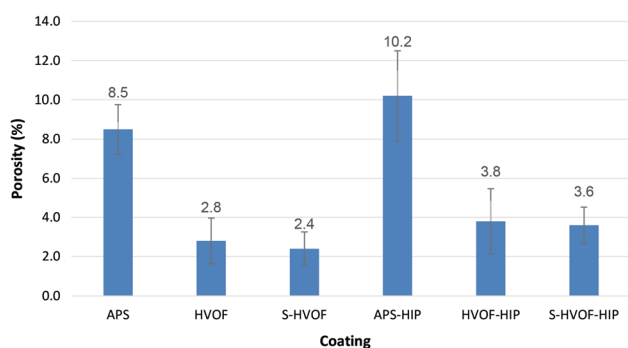


**Fig. 5** Porosity analysis of as-sprayed and HIPed coatings—the porosity in HIPed coatings was determined in areas without any cracks

## Discussion

### Coating Microstructure

#### As-Sprayed Coatings

The APS coating's microstructure has relatively high porosity (Fig. 5) and poor inter-splat bonding compared to the other as-sprayed coatings (Fig. 2a, 4a). The HVOF coating, as observed in Fig. 2(b) and 4(c) has relatively higher inter-lamellar cohesion than the APS coating, which is observable by the distinctness of the horizontal cracks present in both coatings (Fig. 2), and attributed to the high impact velocities and lower temperature of the HVOF spray process. Occasionally, unmolten particles can also occur, as shown in Fig. 2(b). The S-HVOF coating, on the other hand, has a very different microstructure. The powder particles have fused together to form a dense structure with no evidence of intersplat cracking (Fig. 2d), which agrees with the results from Toma et al. (Ref 16, 70, 71). The APS and HVOF coatings' splat thickness is similar in size despite the feedstock powders having large differences in size. This is due to a combination of factors such as the in-flight temperatures and impact velocities, where particle temperature is generally higher and velocity lower in APS compared to HVOF spraying (Ref 76).

#### Phase Compositions

The diffraction patterns presented in Fig. 6(a–c) indicate that all three coatings contain both  $\alpha$ - $\text{Al}_2\text{O}_3$  and  $\gamma$ - $\text{Al}_2\text{O}_3$ . However, as shown in Table 4, the amount of crystalline phases was very different. For the APS coating, the  $\gamma$ - $\text{Al}_2\text{O}_3$  content was above 90 wt.%, which corresponds to the typical value reported in the literature, e.g., (Ref 20, 21, 77). A columnar structure of the  $\gamma$ - $\text{Al}_2\text{O}_3$  in the splats, as previously reported (Ref 26, 27, 36, 37) was also observed in this study. As the connected texture influences

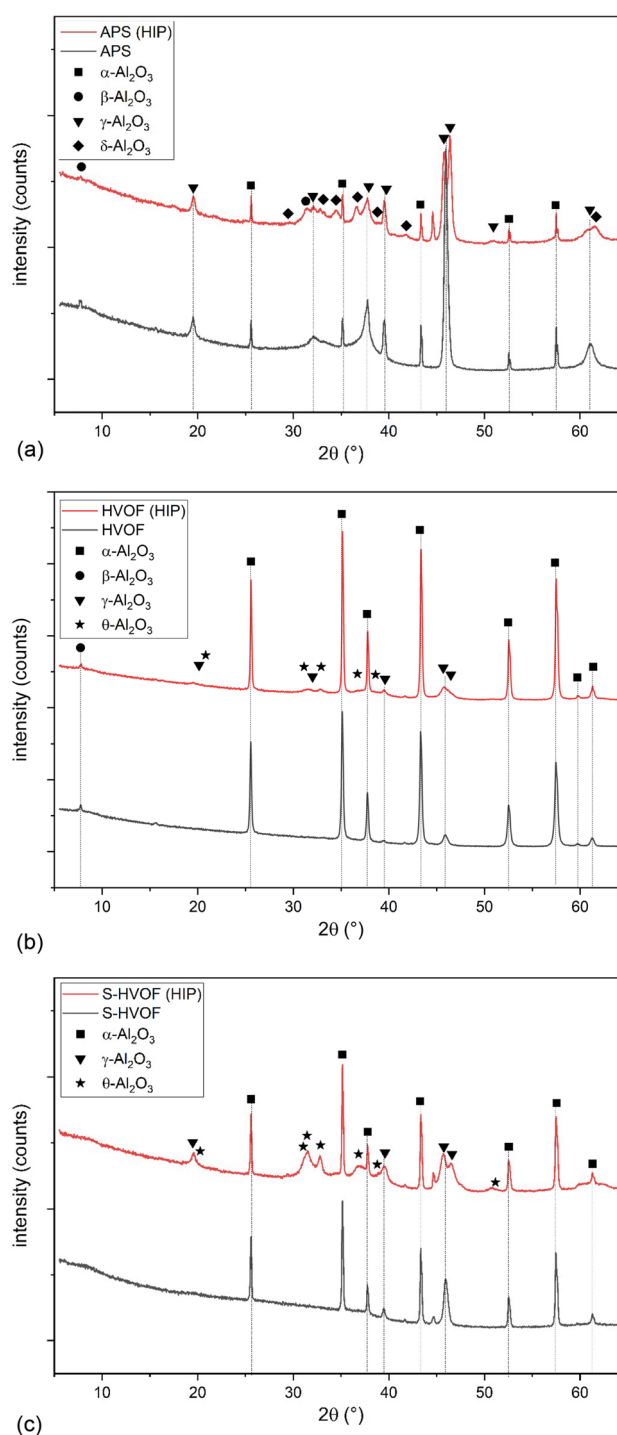


**Fig. 6** XRD analysis of (a) APS and APS-HIP, (b) HVOF and HVOF-HIP, and (c) S-HVOF and S-HVOF-HIP coatings (unmarked peak at  $2\theta$  of  $\approx 44.5^\circ$  is from the substrate)

the result of the quantitative analysis, this effect was considered in this study. The small contents of  $\beta$ - $\text{Al}_2\text{O}_3$  in the APS and HVOF coatings were related to impurities of the feedstock powders (Table 4). Surprisingly, the as-sprayed HVOF coating has a very high content of  $\alpha$ - $\text{Al}_2\text{O}_3$ , i.e.,

**Table 4** Results of the semi-quantitative analysis of the crystalline phase content (wt.%)

Coating	$\gamma$ -Al <sub>2</sub> O <sub>3</sub> , wt%	$\alpha$ -Al <sub>2</sub> O <sub>3</sub> , wt.%	$\delta$ -Al <sub>2</sub> O <sub>3</sub> , wt.%	$\beta$ -Al <sub>2</sub> O <sub>3</sub> , wt.%	$\theta$ -Al <sub>2</sub> O <sub>3</sub> , wt.%
APS	94	6	...	< 1	...
APS-HIP	63	4	33	< 1	...
HVOF	14	85	...	< 1	< 1
HVOF-HIP	25	64	...	< 1	11
S-HVOF	56	44	...	...	...
S-HVOF-HIP	60	21	...	...	19

above 80 wt.%, confirming the results reported in earlier studies (Ref 72-74). However, the microstructure in Fig. 2(b) does not show an unusual amount of unmelted particles, which might be expected from the XRD result (Fig. 6 and Table 4). The  $\alpha$ -Al<sub>2</sub>O<sub>3</sub> content in the S-HVOF coating is consistent with previous studies in suspension spraying of alumina coatings (Ref 46, 71).

HIPing at 910 °C resulted in significant changes in the coating phase composition, as indicated by the diffraction patterns in Fig. 6(a-c) and the results summarized in Table 4. Only after HIP treatment of the APS coating at 910 °C,  $\delta$ -Al<sub>2</sub>O<sub>3</sub> was observed in the coating, while for both other coatings,  $\theta$ -Al<sub>2</sub>O<sub>3</sub> was found. This is surprising for a short treatment time, as the latter phase is most often described for higher heat treatment temperatures (Ref 35, 38). Both the HVOF and S-HVOF coatings behave unexpectedly. The  $\alpha$ -Al<sub>2</sub>O<sub>3</sub> content decreases, and besides the appearance of  $\theta$ -Al<sub>2</sub>O<sub>3</sub>, the  $\gamma$ -Al<sub>2</sub>O<sub>3</sub> content increases. This can be explained by the existence of significant amounts of an amorphous/nanocrystalline phase in the as-sprayed coatings, which crystallizes to different phases during the HIP treatment. The amorphous phase content in alumina coatings is rarely studied in the literature. The amount of amorphous alumina in an as-sprayed APS coating was found to be 12 wt.% (Ref 77). The amorphous phase content in S-HVOF was mostly found in the range of 15-30 wt.%, while the content of crystalline  $\alpha$ -Al<sub>2</sub>O<sub>3</sub> was  $\leq$  6 wt.% (Ref 37). In another study, for S-HVOF coatings an amorphous phase content even up to 74 wt.% depending on the combustion power was determined (Ref 57). Interestingly, even with a very high amorphous phase content, the main crystalline phase can be  $\alpha$ -Al<sub>2</sub>O<sub>3</sub> (Ref 32). Remarkably, Bolelli et al. (Ref 37) reported a direct crystallization of  $\delta$ -Al<sub>2</sub>O<sub>3</sub> from the amorphous phase, but they did not observe  $\theta$ -Al<sub>2</sub>O<sub>3</sub> as an intermediate phase before complete transformation to  $\alpha$ -Al<sub>2</sub>O<sub>3</sub>. Thus, a full understanding of the phase transformation of as-sprayed coatings to fully crystalline  $\alpha$ -Al<sub>2</sub>O<sub>3</sub> coatings requires additional work.

The density of  $\alpha$ -Al<sub>2</sub>O<sub>3</sub> (3.99 g/cm<sup>3</sup>) is higher than  $\gamma$ -Al<sub>2</sub>O<sub>3</sub> (3.6-3.65 g/cm<sup>3</sup>) (Ref 33). This means that there is a volume shrinkage due to the  $\gamma \rightarrow \alpha$  phase transformation during coating heat-treatment. This process leads to coating

cracking as described by Heintze and Uematsu (Ref 21). This volume change will provide a relaxation mechanism at intersplat boundaries for the APS coatings, as the quenching stress at intersplat level is always tensile (Ref 37, 52, 78), leading to lower residual tensile stress, as shown by the experimental values previously reported by the authors and shown here in Fig. 13 (Ref 52) to aid the discussion. This residual stress can also influence the thermal cracking behavior, as observed during the HIPing post-treatment, due to the constrained expansion and contraction of the coating substrate system during the heating and cooling period (Fig. 3). As discussed earlier, a full transformation from  $\gamma$ -Al<sub>2</sub>O<sub>3</sub> to  $\alpha$ -Al<sub>2</sub>O<sub>3</sub> occurs at about 1180 °C (with sufficient heat treatment time) (Ref 33). Hence at the HIP temperature of 910 °C, a complete  $\gamma \rightarrow \alpha$  phase transformation phase transformation could not occur, but the HIPing allowed the formation of nuclei/crystallite formation and growth from the amorphous (nano)phase (Table 4).

#### *Influence of HIPing on Internal Stress*

The cross-sectional images shown in Fig. 3 indicate that HIPing post-treatment caused a varying degree of microcracking in the coating microstructure. During the HIPing post-treatment, microcracking led to the delamination of parts of the coating for the S-HVOF-HIP coating (Fig. 3f). Vertical cracking was also observed in the case of HVOF-HIP coating (Fig. 3d, 9e(1)); however, no coating delamination was observed in this case. In the case of APS-HIP coatings, despite significant surface cracking which was removed by grinding leading to a significantly lower coating thickness (Fig. 3b), no coating delamination was observed after HIPing. As the HIPing conditions of heating/cooling rate and the hold time were the same for all coatings, the residual stresses caused by the mismatch of thermal expansion of the coating and substrate material could induce relatively more significant cracking in the case of the relatively dense structure of HVOF-HIP and S-HVOF-HIP coatings (Fig. 2). The relatively poor intersplat bonding (Fig. 2a, 4a, b) and higher porosity (Fig. 5) in the case of APS coatings, provided a stress relaxation mechanism to avoid coating delamination during the

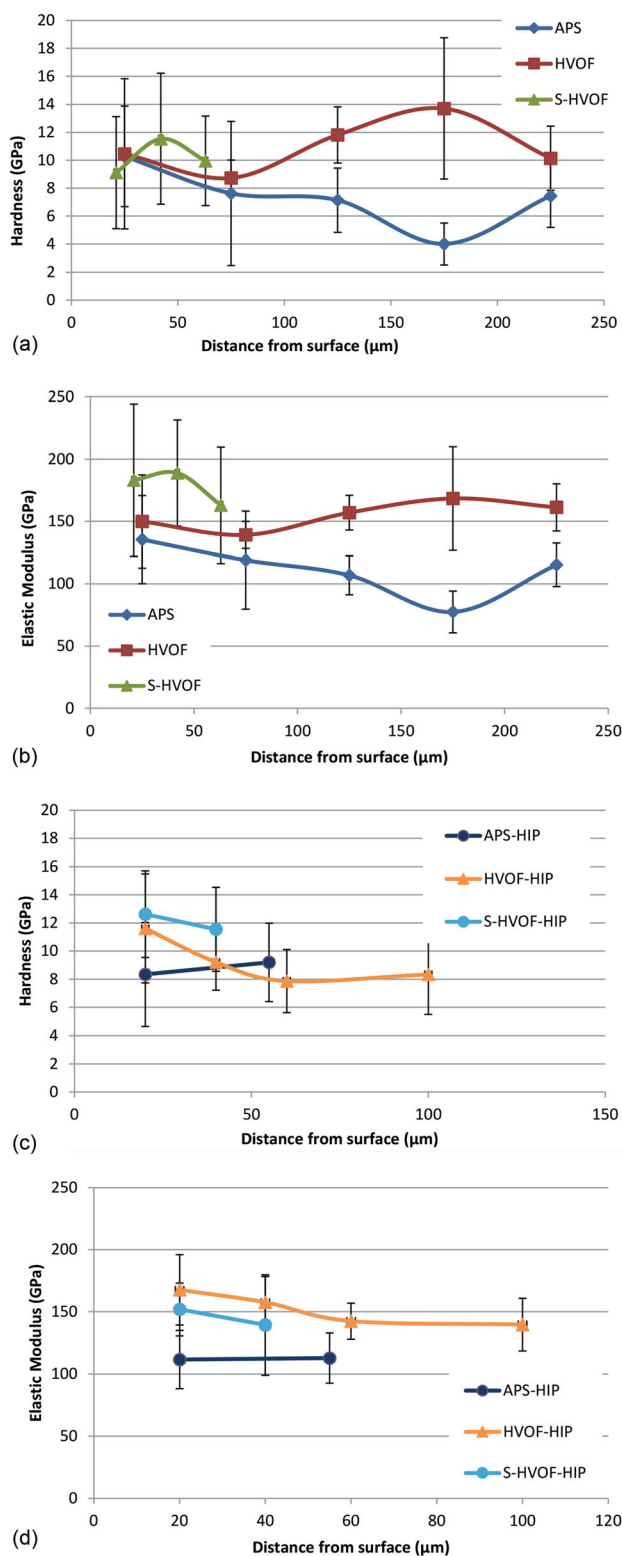


**Fig. 7** Nanoindentation analysis of (a) hardness in as-sprayed coatings, (b) hardness in HIPed coatings, (c) elastic modulus in as-sprayed coatings and (d) elastic modulus in HIPed coatings

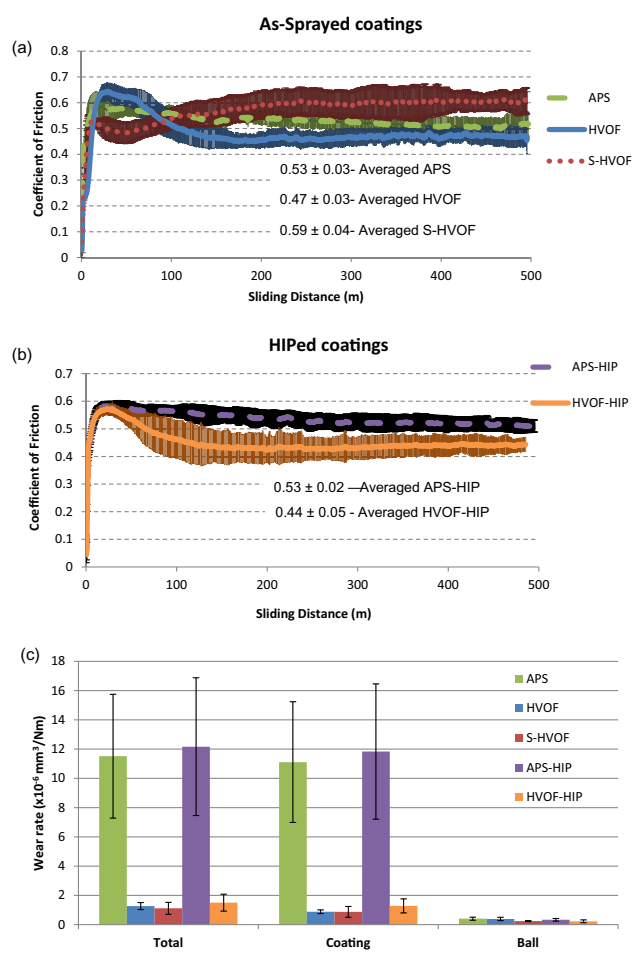


**Fig. 8** (a) Coefficient of friction (CoF) of the as-sprayed coatings, (b) HIP coatings, (c) Wear performance of the coating showing total, coating and counter-body (ball) wear rates. The averaged steady state CoF values for the last 300 m of sliding distance are also given in Figures (a) and (b)

**Table 5** Summary of ball and coating wear loss after sliding wear results

Coating	Wear rate, × 10 <sup>-6</sup> mm <sup>3</sup> /Nm		
	Total	Coating	Ball
APS	11.52 ± 4.23	11.11 ± 4.13	0.41 ± 0.10
HVOF	1.27 ± 0.24	0.88 ± 0.12	0.39 ± 0.12
S-HVOF	1.12 ± 0.41	0.87 ± 0.37	0.24 ± 0.04
APS-HIP	12.17 ± 4.71	11.83 ± 4.62	0.33 ± 0.09
HVOF-HIP	1.50 ± 0.58	1.28 ± 0.48	0.23 ± 0.10

HIPing post-treatment. Volume changes caused by the phase transformations during HIPing (Table 4) also contributed to the cracking behavior.

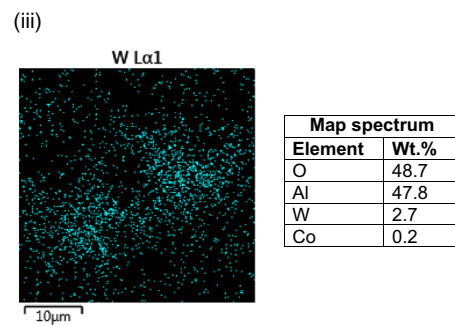
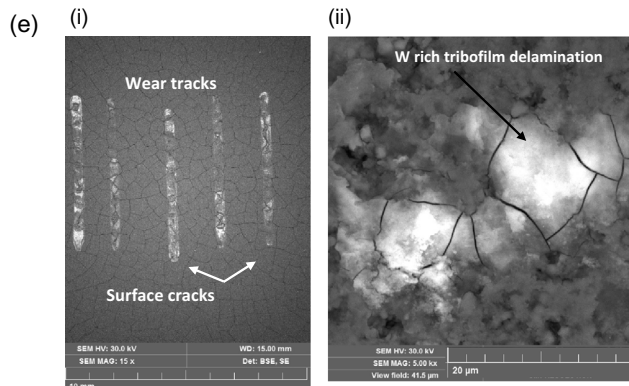
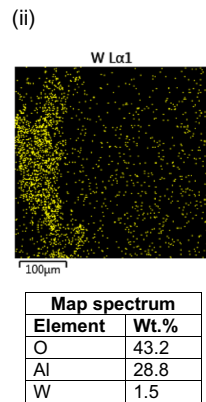
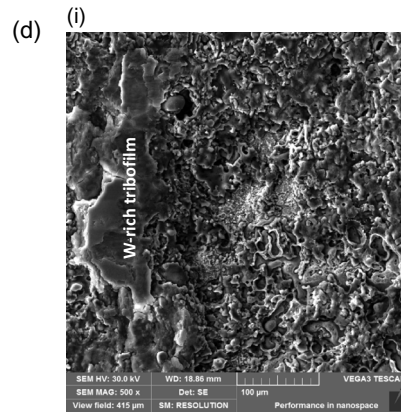
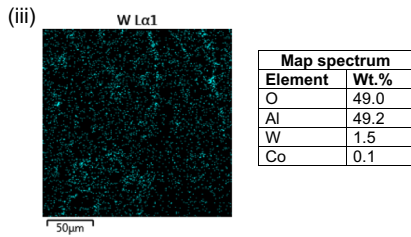
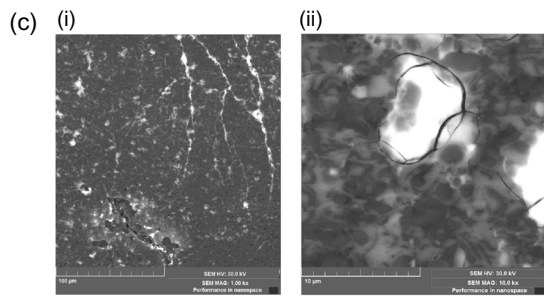
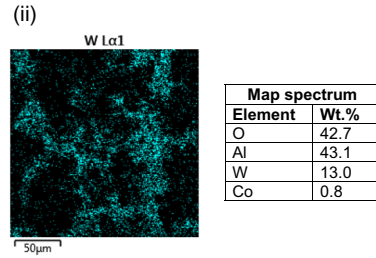
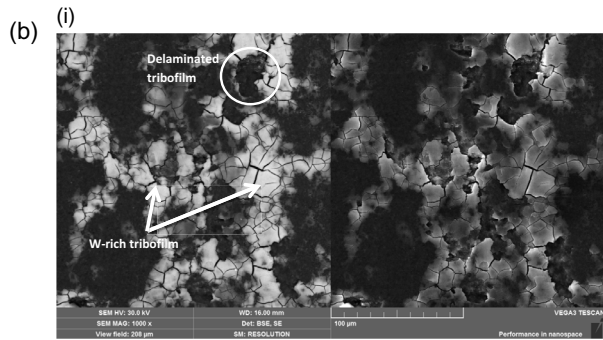
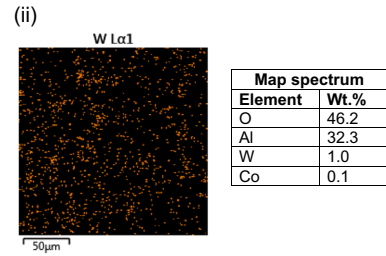
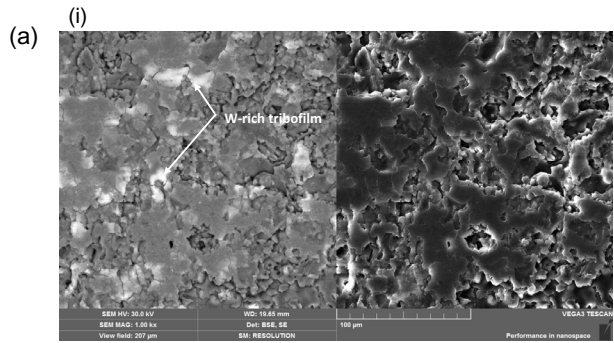




**Fig. 9** BSE images of wear track with EDS map of W of (a) APS (i) BSE and SE mode, respectively, (ii) EDS map of (i); (b) HVOF (i) BSE and SE mode, respectively, (ii) EDS map of (i); (c) S-HVOF (i) BSE, (ii) BSE (higher magnification), (iii) EDS map of (i); (d) APS-HIP (i) SE, (ii) EDS map of (i); (e) HVOF-HIP coatings (i) BSE, (ii) BSE (higher magnification), (iii) EDS map of (ii)

Previously, the authors conducted a through-thickness residual stress profile investigation of the as-sprayed APS and HVOF coatings using the non-destructive neutron diffraction method (Fig. 13) (Ref 52). These measurements provide an understanding of the influence of residual stress during sliding contact. The externally applied stress during the sliding wear test is superimposed on the existing residual stress profile in the coating substrate system. Compressive residual stress is therefore preferred to resist crack initiation and propagation in engineering materials, e.g., gears are shot-peened to induce compressive residual stress in the near-surface region to improve fatigue life (Ref 79). Experimentally measured through-thickness residual stress profile in the APS and HVOF coatings in Fig. 13 indicates that the residual stress in the APS coating was tensile. In contrast, the residual stress in the HVOF coating was predominantly compressive.

As discussed above, after HIPing, all coatings cracked (Fig. 3), and hence any build-up of residual stress during this post-treatment was released by the onset of cracks. The APS-HIP coating cracks were near-surface and removed by grinding and polishing before sliding wear tests. Hence these cracks are not observed in Fig. 3(b). Although the severity of cracking after HIPing varied between the three coatings, it would not be possible to experimentally measure the *in-situ* evolution and build-up of residual stress during high temperature HIPing treatment, prior to cracking, using existing destructive and non-destructive measurement techniques (Ref 79). Experimental residual stress measurement of cracked HIPed coatings would be misleading, as delamination and cracking of coatings would release stress. However, it is possible to approximate the build-up of residual stress prior to cracking using mathematical models based on the difference in the coefficient of thermal expansion, as initially proposed by Gill (Ref 80). The in-plane thermal residual stresses produced in a thin coating attached to a thick substrate can be approximated using the difference in the coefficient of thermal expansion (CTE) of the coating substrate system (Ref 78).

$$\hat{\sigma}_c = E_c \Delta T (\text{CTE}_s - \text{CTE}_c) \quad (\text{Eq 1})$$

where  $\hat{\sigma}_c$  is the residual stress in the coating,  $E_s$  is the Young modulus of the coating,  $\Delta T$  is the temperature change, and  $(\text{CTE}_s - \text{CTE}_c)$  represents the difference in the CTE of the underlying substrate and coating. Subscripts

$c$  and  $s$  relate to the material's properties for the coating and the substrate, respectively.

The CTE of  $\text{Al}_2\text{O}_3$  ranges from  $7.10 \times 10^{-6}$  to  $10.59 \times 10^{-6} \text{ K}^{-1}$  at temperatures of 127–1327 °C, respectively, whereas the AISI 440C steel substrate has the averaged value of  $11.2 \times 10^{-6} \text{ K}^{-1}$  in the temperature range of 20–600 °C (Ref 20). Although these CTE values are temperature and phase-dependent, they can provide a benchmark for residual stress calculations. The above CTE values do not consider any changes in alumina's phase composition during HIPing (Table 4) or spraying (Fig. 6). As the  $\text{CTE}_{\text{substrate}} > \text{CTE}_{\text{coating}}$ , the substrate contracts more than the coating during cooling and hence the in-plane residual stress in the coating should be compressive after thermal spraying and also HIPing. Although the as-sprayed HVOF coating showed compressive residual stress, as shown in Fig. 13, the APS coating shows tensile residual stress. This difference in behavior is attributed to the poor intersplat bonding and relatively higher porosity in the APS coating (Fig. 2a, 4a), which provides a mechanism to relieve the expected compressive residual stress during coating build-up.

After the coatings are HIPed, the expected magnitude of compressive residual stress in the coatings based on Eq. 1 can be approximated as 312 MPa, for  $E_c = 150 \text{ GPa}$  as an approximation from Fig. 7,  $\Delta T = 885 \text{ °C}$ ,  $\text{CTE}_s = 11.2 \times 10^{-6} \text{ K}^{-1}$  and  $\text{CTE}_c = 8.84 \times 10^{-6} \text{ K}^{-1}$  (averaged value). This magnitude of residual stress can lead to microcracking in the absence of a stress relief mechanism. For the case of APS coatings, it is postulated that poor intersplat bonding and porosity provided this relief mechanism during HIPing post-treatment (Fig. 4b, 5). Hence, no macrocracking and delamination were observed after the heat-treatment. However, as the coating density in the case of HVOF coating was higher (Fig. 5) due to a relatively smaller number of pores and cracks (Fig. 2, 3, 4), the stress builds up in the coating during HIPing, as there was limited relief at the intersplat boundaries and pores; leading to cracking within the coating microstructure (Fig. 4b). In the case of S-HVOF coatings with relatively high density and finer structure, it is postulated that there was no relief mechanism due to microcracking during the build up of residual stress during HIPing, leading to a gradient of residual stress at the coating substrate interface and thus partial delamination of small coating segments (Fig. 3f). Based on the above mathematical model (Eq 1), all coatings prior to cracking during the HIPing treatment were expected to be in compressive residual stress. This is shown schematically in Fig. 14. The interface represents a sharp change of residual stress from compression to tension, resulting in coating delamination. Owoseni et al. (Ref 18) also considered the heat treatment of suspension alumina coatings in the temperature range of 600–750 °C to

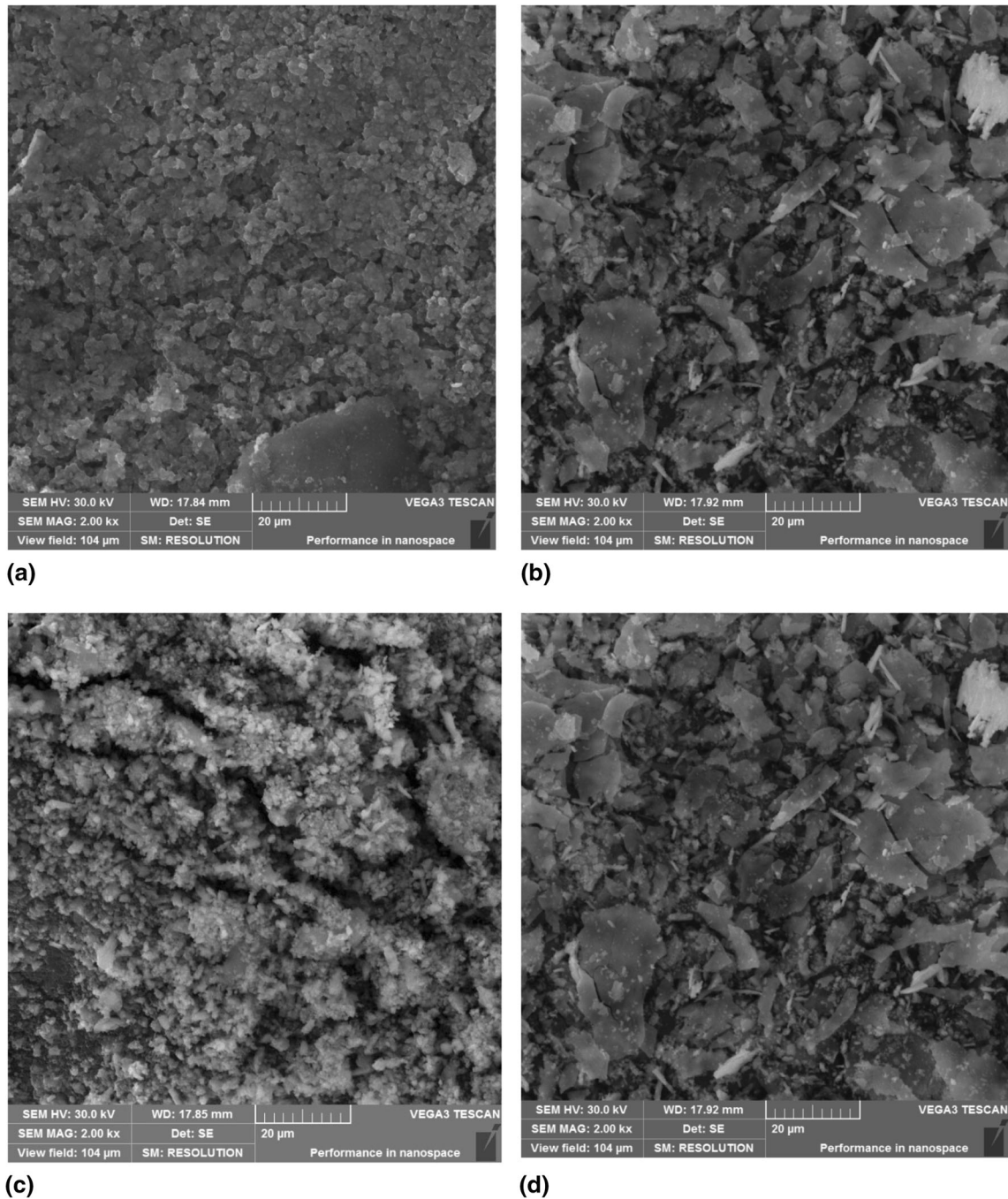


**Fig. 10** SEM images of sliding wear debris from (a) APS, (b) HVOF, (c) APS-HIP and (d) HVOF-HIP coatings

investigate phase changes and their influence on sliding wear performance. They indicated that regardless of the heat-treatment time, it resulted in a range of cracks in web-like formation, similar to the observation shown in Fig. 9e(i) in the current investigation. Although the above analysis of residual stress did not consider the phase transformation changes and content of the amorphous

phase, it provides a benchmark of expected residual stress values during HIPing.

Equation 1 can also be applied to approximate residual stress build-up between the coating and substrate material during coating deposition. As shown in Fig. 13, the compressive residual stress in the as-sprayed HVOF coating shows a value of 200 MPa, whereas the APS coating has a tensile stress of 50 MPa near the interface (Fig. 13). For a

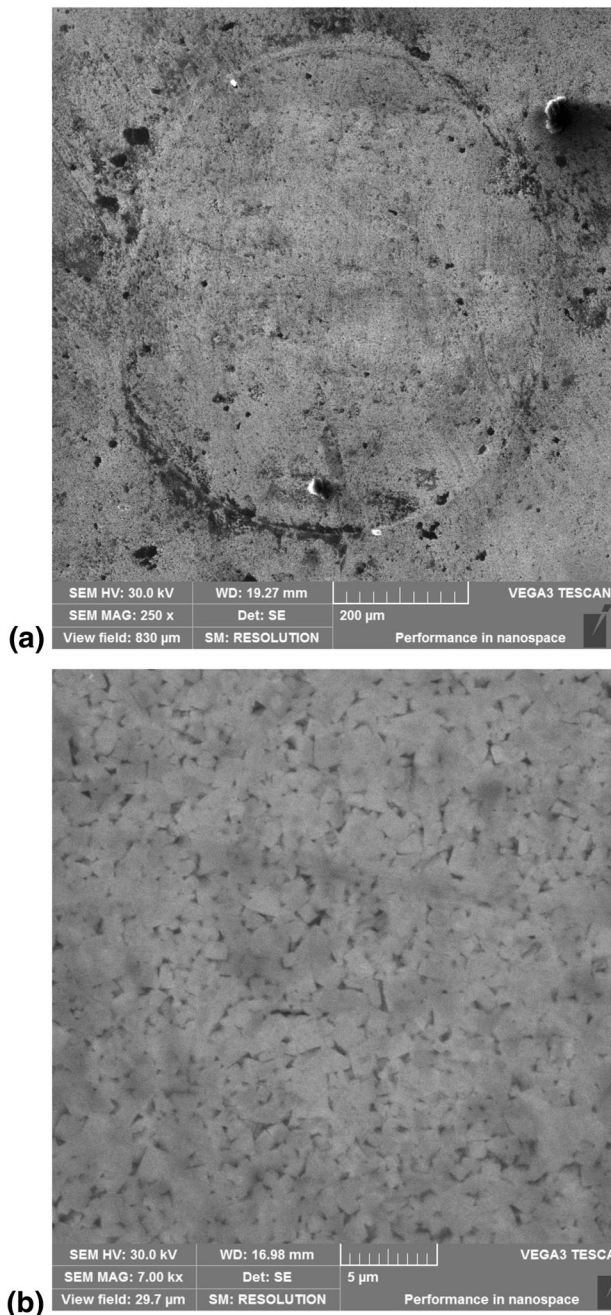


**Fig. 11** SEM images of WC-6Co ball wear scar for the APS coating test couple (a) low magnification, (b) high magnification

compressive residual stress of 200 MPa in the HVOF coating, it can be calculated from Eq 1 that the coating deposit and substrate reached an average temperature difference ( $\Delta T$ ) of 565 °C during coating deposition. Although there will be a temperature difference between the deposition conditions of the APS and HVOF coatings, as a first approximation, they can be assumed similar, and a tensile residual stress of 50 MPa in the APS coating shows

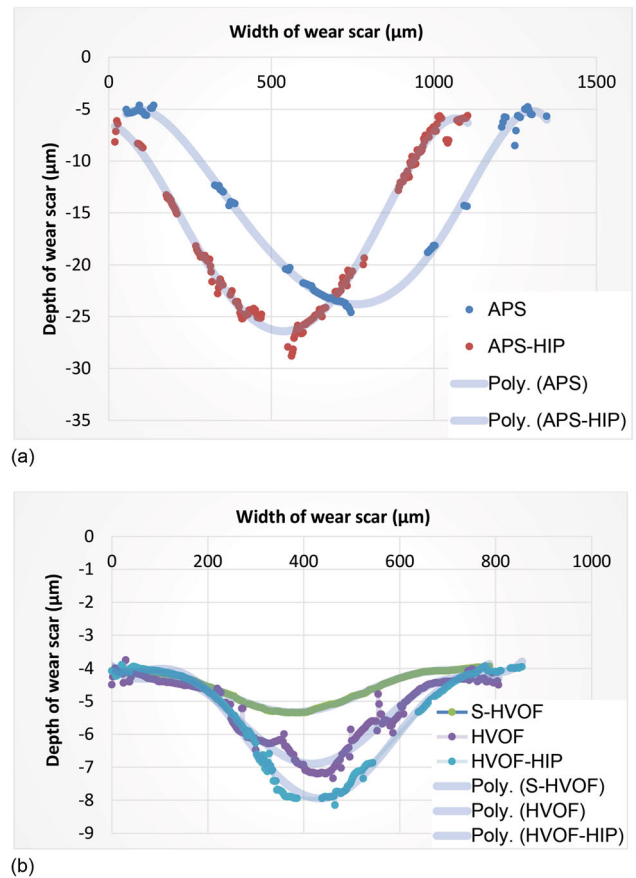


**Fig. 12** A comparison of wear track depth and width profiles of (a) APS and APS-HIP, and (b) HVOF, S-HVOF, HVOF-HIP coatings

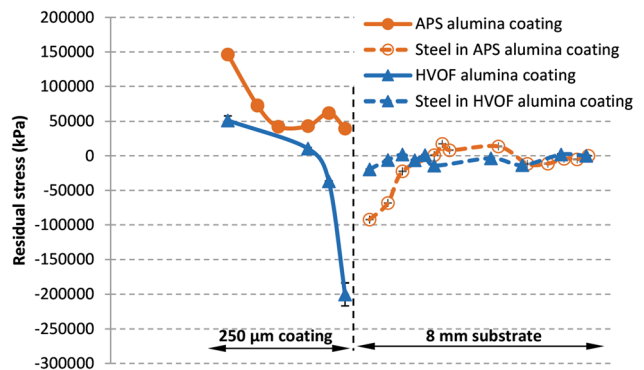
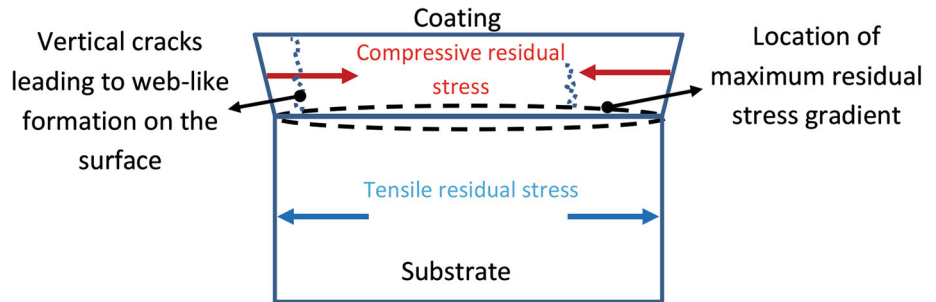


**Fig. 13** Through thickness neutron diffraction residual stress results for APS and HVOF alumina coatings (Ref 52). Reprinted from R. Ahmed, N. H. Faisal, A. M. Paradowska, and M. E. Fitzpatrick, Residual strain and fracture response of Al<sub>2</sub>O<sub>3</sub> coatings deposited via APS and HVOF techniques, Journal of Thermal Spray Technology, Vol. 21, pg. 23-40, 2012, Springer Nature

that the residual stress was released after spraying. Therefore, it is postulated that the relatively poor intersplat bonding and porosity in the APS coating provided a stress relief mechanism during the coating deposition (Fig. 3, 4, 13) and HIPing process.

**Fig. 14** Schematic of interfacial stress gradient for alumina coating where  $CTE_s > CTE_c$ , leading to delamination at the coating substrate interface and cracking within the coating



## Hardness and Elastic Modulus

In the absence of plasticity, the dominant material deformation mechanism in Vickers indentation was micro- and macro-cracking and chipping for alumina coatings (Ref 51). Nanoindentation hardness analysis presented in Fig. 7(a) indicated that the hardness of the HVOF and S-HVOF coating was, on average  $\approx 10$  GPa, whereas it was lower  $\approx 7.3$  GPa for the APS coating. The high standard deviation of averaged values in Fig. 7 was attributed to the coatings' phase variations and microstructural features (Fig. 2, 3, 4, 6 and Table 4). Relatively lower hardness of the APS coating in comparison to the HVOF and S-HVOF coatings was attributed to four factors, (1) a high  $\gamma$ - $Al_2O_3$  content (Fig. 6, Table 4), (2) poor intersplat bonding and cracks in the microstructure reducing the stiffness of the indenter-coating-substrate system (Fig. 2a, 4a), (3) relatively higher porosity (Fig. 5), (4) relatively higher value of tensile residual stress increasing the tendency of microcracking during the indentation process (Fig. 13). Values of hardness for HVOF and S-HVOF coatings reported here were consistent with a value of 9 GPa reported for suspension sprayed alumina by Owoseni et al. (Ref 18), and HVOF-sprayed conventional and nanocoatings reported by Bolelli et al. in the range of 10.0–10.2 GPa (Ref 66). The hardness value for the APS coating was lower than 9.3 and 11.7 GPa in Ref 66 and 67, respectively. These differences in nanohardness between the as-sprayed coatings were attributed to the differences in the deposition process and process parameters during spraying. The nanohardness of both HVOF and S-HVOF coating increased after HIPing to values in the range of 11.6–7.9 and 12.6–11.5 GPa, respectively. After the HIPing post-treatment, the relative hardness of the APS-HIPed coating also changed in the near surface region to values between 8.3 and 9.2 GPa. These changes are attributed to the phase transformations during HIPing (Fig. 6, Table 4).

At the microhardness level, the values of HVOF ( $632 \pm 29$  HV0.2) were closer to APS ( $683 \pm 38$  HV0.2) coatings, which was not the case for the nanohardness measurements. This difference was attributed to the local variations in the hardness within the microstructure, which

was averaged during each microhardness measurement due to the indentation size effects. Nevertheless, the low microhardness of the HVOF coating was surprising, with respect to the high content of  $\alpha$ - $Al_2O_3$  (Table 4) and low coating porosity (Fig. 5). Vickers microhardness values of alumina coatings reported here were on the lower bound range of hardness values, compared to the range of Vickers hardness values of 765–1326 HV reported in published literature (Table 1). The variation in these values in the current investigation (Fig. 7) was probably due to microstructural differences caused by the feedstock, spray process, spray parameters and hardness test conditions. Therefore, the resulting phase composition and microstructural features play an important role.

Indentation elastic modulus indicates the measurement of system's stiffness, where the indenter, coating and substrate are in series (Ref 81). It is a measure of the microstructural stiffness, which in this case is also dependent upon the intersplat bonding. Although there were microstructural variations within the deposited coating, a change in the averaged elastic modulus values, reflect a change in the overall stiffness. The results presented in Fig. 7(b) indicated that the S-HVOF coating's dense microstructure had the highest intersplat bonding resulting in the highest modulus value in the range of 160–180 GPa. This was followed by the modulus of HVOF coating, which indicated values of 140–175 GPa. Due to poor intersplat bonding, higher porosity and a high  $\gamma$ - $Al_2O_3$  content, the APS coating had the lowest modulus range of 77–135 GPa. After the HIPing post-treatment, although the APS-HIP coating was thinner due to grinding to eliminate the surface cracks (Fig. 3b), there was a decrease in the intersplat bonding, as indicated by a modulus of 112 GPa. This could be associated with the still high  $\gamma$ - $Al_2O_3$  content and defects such as interlamellar cracks and porosity, which restricted the intersplat bonding during the HIPing post-treatment. For HVOF-HIP coatings, there was an increase in near-surface elastic modulus from 150 to 167 GPa, whereas the S-HVOF-HIP coating showed a decrease in the near-surface elastic modulus from 180 to 151 GPa. These changes in elastic modulus follow a trend

of the extent of cracking after HIPing, as indicated in Fig. 3, 4.

### Sliding Wear Resistance

Sliding wear rates shown in Fig. 8(c) indicate that the APS coating has the highest wear rate, which was an order of magnitude higher than for the HVOF and S-HVOF coatings. The S-HVOF coating had the highest wear resistance among the test couples considered in this investigation. The total wear rate was dominated by the coating wear rate, as the ball wear rate was relatively low (Table 5). After the HIPing post-treatment, there was an increase in the average total wear rate of 5.6% and 18% for the APS-HIP and HVOF-HIP coatings, respectively. This increase in the average value was within the standard deviation of the results shown in Fig. 8(c). In the study reported in Ref 18, although the feedstock was not  $\alpha$ -alumina, it was reported that at a low heat-treatment temperature of 600 °C, there was a decrease in the wear rate of about 47%; however, the wear rate increased by orders of magnitude when the coating was heat-treated at 750 °C. Hence, the wear performance is dependent on the heat-treatment temperature. After the running-in stage, the steady-state CoF was the highest for the S-HVOF coating, followed by APS and then HVOF in the as-sprayed test couples. There was no significant relative difference in the steady-state CoF values after the HIPing post-treatment.

The sliding wear resistance of alumina coatings depended on the coating microstructure, phase composition and tribological test parameters. This resulted in orders of magnitude variations in the wear rate ( $\text{mm}^3/\text{Nm}$ ), as summarized in Table 1. However, some parallels can be drawn from the tests conducted using the reciprocating ball on flat tests in Table 1 (Ref 18, 57, 59, 60) and this study. Although the counterbody in all of these ball on flat tests is alumina (Table 1) instead of WC-Co used in the current study, Ref 57 and 60 indicated a wear rate in the range of 0.2 to  $11.2 \times 10^{-6} \text{ mm}^3/\text{Nm}$ , which was similar to the values of 0.8 to  $11.8 \times 10^{-6} \text{ mm}^3/\text{Nm}$  in the current study; except for the 101 kW S-HVOF coatings in Ref 57, where a wear rate was of  $40\text{--}44 \times 10^{-6} \text{ mm}^3/\text{Nm}$ . Ref 18 reported wear rates in the range of 0.0029 to  $\sim 1 \times 10^{-6} \text{ mm}^3/\text{Nm}$  for alumina coatings. However, this comparison needs to be considered with caution, as the test load in these tests was relatively low, i.e., between 2 and 16 N (Ref 18, 59, 60), and the sliding distance in Ref 18 was only 36 m, instead of 500 m used in the current study. For the case of Ref 59, the reported wear rate for the APS coating was orders of magnitude higher in the range of  $315 \times 10^{-6} \text{ mm}^3/\text{Nm}$  to  $1259 \times 10^{-6} \text{ mm}^3/\text{Nm}$  than the other studies reporting on similar tests for these coatings. The test load, in this case, was 2 N, with a total sliding distance of 378 m,

which was lower than the test parameters used in the current study. The high wear rates observed in Ref 59 can be attributed to the coating microstructure. A similar order of magnitude variation in alumina coatings' wear rate was also observed for the unidirectional pin on disk or ball on disk test conditions, as summarized in Table 1.

### Wear Track Observations

Figure 9 shows the SEM observations of the worn wear tracks in both SE and BSE modes. Two features are evident from these observations. The first is W-rich transfer film presence on coatings' surface, as seen in the BSE images and associated tungsten maps. In some cases, e.g., Figure 9(b), the W-rich transfer film covered a significant portion of the observed wear track, whereas in Fig. 9(a), small islands of the W-rich transfer film can be observed. The EDS map spectrum indicated that tungsten ranges from 1 to 13 wt.%. The second feature was the presence of microcracks in the coating leading to the removal of material. The SEM observations at various magnifications did not indicate any plasticity or abrasive marks on the wear tracks' surface. The microfractured surfaces look rough, whereas the W-rich film presented a smooth surface (Fig. 9).

The observations of the wear debris in Fig. 10 indicate delaminated fragments of coatings. In the case of APS and APS-HIP coating, the debris fragments were finer (Fig. 10a, c), indicating that they were trapped within the wear track and ground to finer particles during the sliding wear process. This was consistent with the depth and width analysis of the wear track profile shown in Fig. 12(a), where the wear scar was significantly deeper and wider compared to other test couples. Once the debris was trapped, it influences both the friction and wear behavior in the form of three-body wear. In the case of HVOF and S-HVOF coatings, the depth of the wear scar, as well as the morphology of the delaminated debris shown in Fig. 10(b and d) indicate that the delaminated debris was pushed from the wear track because of its relatively lower depth (Fig. 12); the friction and wear mechanism was two-body and three-body wear. SEM observations of the wear track on the WC-Co ball counterpart did not reveal any abrasive marks or transfer material (Fig. 11).

### Wear Mechanism

The wear resistance of thermal spray coatings depends on their mechanical properties, such as hardness, toughness, the test couples' elastic modulus, and the tribological test conditions of stress, sliding velocity, and properties of the counterbody (Ref 76). Table 1 indicates that other studies have considered the sliding wear of the alumina coatings

against different counterbodies, such as sintered alumina, steel (100Cr6, EH32), and SiC. Deng et al. (Ref 82) showed that the counter body's tribomechanical properties significantly influence the wear mechanism of the test couples. They conducted a comparative study of plasma-sprayed alumina coatings sliding against ZrO<sub>2</sub>, Si<sub>3</sub>N<sub>4</sub>, Al<sub>2</sub>O<sub>3</sub> and stainless steel balls using a ball-on-disk tribometer. Their investigation concluded that alumina coating sliding exhibited diverse tribological behavior, which was attributed to the differences in the mechanical and tribochemical properties of the counterbody. Moreover, these authors reported the transformation of  $\gamma$ -Al<sub>2</sub>O<sub>3</sub> to  $\alpha$ -Al<sub>2</sub>O<sub>3</sub> due to frictional contact during sliding. There are no reported studies of pure alumina coatings sliding against a WC-Co counterbody (Table 1) in published literature; however, few investigations considered the sliding wear of binary Al<sub>2</sub>O<sub>3</sub>-TiO<sub>2</sub> coatings against WC-Co counterbody (Ref 83-85). WC-Co counterbodies reduce friction and wear by the formation of a W-rich tribofilm, as reported for APS Al<sub>2</sub>O<sub>3</sub>-13 wt.%TiO<sub>2</sub> and Al<sub>2</sub>O<sub>3</sub>-40 wt.%TiO<sub>2</sub> coatings (Ref 83), suspension sprayed WC-Co coatings (Ref 86, 87) and Stellite alloys (Ref 88).

The current study, which considers WC-Co counterbody, indicates that three factors dominated the wear mechanism of the different alumina coatings, i.e.,

1. Formation of a W-rich tribofilm,
2. Mechanical properties of coatings,
3. Debris interactions in the contact region between the coupled materials.

**W-rich tribofilm** Tribofilms form due to the exchange of materials between the coupled bodies due to flash temperature during asperity contact. The tribofilm can reduce both the CoF and wear rate by acting as a solid lubricant and providing a low-shear strength layer. SEM and EDS analysis of the wear tracks of the coatings showed the presence of tungsten, indicating that the tribofilms formed on the coatings were the cause of asperity interactions and flash temperatures in the presence of oxygen during the sliding wear tests (Fig. 9). Engqvist et al. (Ref 89) have discussed the reactions forming tribofilm consisting of WO<sub>3</sub> for self-mated WC-Co during dry sliding in air and nitrogen environments. In previous studies, authors have also indicated the presence of oxygen-rich tungsten tribofilm for test couples involving WC-based hardmetals (Ref 76, 90). This tribofilm occurs regardless of the microstructural phase of W in the tribo-system (Ref 76). For the case of Al<sub>2</sub>O<sub>3</sub>-TiO<sub>2</sub> coatings sliding against WC-Co counterbody (Ref 83-85), WO<sub>3</sub> tribofilm was reported by Fervel et al. (Ref 83), whereas Guessasma et al. (Ref 84) also reported the formation of a tribofilm. In the current investigation, the extent of this protective W-rich tribofilm varied for different test couples (Fig. 9). There is a

competing mechanism of W-rich tribofilm formation and removal during the sliding wear process. Once the film is formed, it grows until the shear stress within the contact region exceeds the shear strength of the film, leading to the removal of tribofilm. This triggers the formation of the new tribofilm due to asperity interaction.

The amount of tribofilm formation was relatively higher for the HVOF and HVOF-HIP tests (Fig. 9b, e) compared to the APS and APS-HIP coatings (Fig. 9a, d). There was also tribofilm formation in the case of S-HVOF coating, as observed in the tungsten map and high-resolution image (Fig. 9c); however, this film's intensity in the wear track was lower than the HVOF coatings. Therefore, it is postulated that the relatively higher content of the  $\alpha$ -Al<sub>2</sub>O<sub>3</sub> in the HVOF and S-HVOF coatings (Table 4) promotes a more stable W-rich tribofilm formulation. This was consistent with the findings of Deng et al. (Ref 82), which indicated  $\alpha$ -Al<sub>2</sub>O<sub>3</sub> as a stable phase during sliding wear, and the authors concluded the transformation of  $\gamma$ -Al<sub>2</sub>O<sub>3</sub> to  $\alpha$ -Al<sub>2</sub>O<sub>3</sub> due to frictional contact in the sliding wear process. However, this needs to be considered in combination with the high wear rate for the APS and APS-HIP coatings, which can destabilize the tribofilm due to fracture of underlying coating material and wear debris entrapment in the wear track, as discussed in the next sections.

**Coating fracture** The hardness of the sintered WC-Co ball is Rockwell 'A' 90.5-91.5 (Table 3), which was significantly higher than the average hardness of all coatings in this study (Fig. 7 and Sect. 4.3). The fracture toughness of alumina thermal spray coatings was also limited, typically in the range of 2.3-3.5 MPa m<sup>1/2</sup>, respectively, for the APS and HVOF coatings (Ref 51), which is significantly lower than for the sintered WC-Co (Ref 76). Fracture toughness values in Ref 51 were similar to the published literature values for alumina coatings (Table 1), with a range of 0.8-2.8 MPa m<sup>1/2</sup>. Low fracture toughness of alumina coatings triggers micro- and macro-fracturing under the contact stress and asperity interaction during the sliding wear process.

Table 1 shows high variations in the wear rate (0.001 to 1259 × 10<sup>-6</sup> mm<sup>3</sup>/Nm) for plain alumina coatings due to the changes in deposition conditions (e.g., Ref 57, 59, 60, 64), heat treatment (e.g., Ref 18) and powder size, e.g., Ref 61, 66, as well as tribological test conditions. In conclusion, improving the sliding wear performance of alumina coatings requires further research, as the current results indicate that factors such as powder size, spray process, spray parameters, and sliding wear test conditions can have a more significant influence than additions of a second oxide, e.g., for Al<sub>2</sub>O<sub>3</sub>-TiO<sub>2</sub> (Ref 67, 83, 85, 91, 92) the sliding wear rates of binary Al<sub>2</sub>O<sub>3</sub>-13 wt.% TiO<sub>2</sub> coatings have been reported as ~0.013 × 10<sup>-6</sup> mm<sup>3</sup>/Nm (Ref 92), ~117 to 472 × 10<sup>-6</sup> mm<sup>3</sup>/Nm (Ref 67) and

$\sim 20$  to  $120 \times 10^{-6}$  mm<sup>3</sup>/Nm (Ref 85). The same conclusion can be drawn when comparing the wear rate of other binary compositions such as Al<sub>2</sub>O<sub>3</sub>-ZrO<sub>2</sub> (Ref 62), Al<sub>2</sub>O<sub>3</sub>-SiO<sub>2</sub> (Ref 93), Al<sub>2</sub>O<sub>3</sub>-SiC (Ref 63), and Al<sub>2</sub>O<sub>3</sub>-YSZ (Ref 63).

As depicted in the current work, residual stress is another factor influencing the wear mechanism. The residual stress profiles (Fig. 13) indicate that the alumina APS coating had high tensile stress, whereas the HVOF coating had compressive residual stress. A compressive residual stress is advantageous in combatting fracture and fatigue failure by reducing the tensile stress field responsible for crack initiation and propagation. Tensile residual stress in the APS coating does not resist crack initiation and propagation. Relatively lower hardness, fracture toughness, and poor intersplat bonding (Fig. 2a, 4a) of the APS coatings thus indicate its lower resistance to fracture and delamination during the sliding wear process. As discussed above, this lower coating quality is linked to the higher  $\gamma$ -Al<sub>2</sub>O<sub>3</sub> content of the APS coating and tensile residual stress. Similarly, the relative lower velocity of the impacting lamella in APS coatings led to poor intersplat strength (Fig. 2a, 4a). Higher mechanical strength of the HVOF and S-HVOF coatings (nanohardness and elastic modulus) and a finer and dense microstructure resulted in the highest wear resistance. This is consistent with the relatively smooth wear track surface of the S-HVOF coatings with no significant fracture.

**Debris interaction** The wear debris' entrapment in the APS and APS-HIP coating test couples' deeper wear groove led to finer debris (Fig. 10). This also changed the wear process to predominantly three-body wear. The rolling and sliding of trapped wear debris in the APS coatings' deep wear groove further increased the coating wear due to local stress concentration originating from the asperity contact on the coating and debris surface (Fig. 12). As the entrapped debris in the case of APS and APS-HIP coating was predominantly alumina coating particles since the WC-Co ball wear was very low in all cases (Fig. 8c), the contact became predominantly alumina coating—alumina coating debris. As the entrapped debris is crushed within the contact zone, its fracture toughness increases due to finer size and hardness vary depending upon the phase composition of its constituents. The shape of the debris increases the contact stress as debris protrusions decrease the real area of contact, accelerating coating wear. As the contact becomes predominantly alumina coating—alumina coating debris, the WO<sub>x</sub> tribofilm formation on the coating surface caused by the WC-Co counterbody becomes unstable, as indicated by the relatively lower concentration and isolated locations of W-rich tribofilm (Fig. 9), which further accelerates APS and APS-HIP coating wear rate.

The entrapment of debris also influenced the wear rate and mechanism of the WC-Co ball (Fig. 11). There was no evidence of abrasion marks on the WC-Co ball's worn surface, which is attributed to its high hardness. Even the sintered alumina's hardness ranges from 1250 to 1500 HV, which is lower than the WC-Co ball (Ref 76). Similarly, the fracture toughness of sintered alumina is lower than the WC-Co ball (Ref 76). Hence, even if the alumina debris from the coating shows higher toughness due to finer particles and a hardness dominated by the  $\alpha$ -alumina wear particles, its mechanical strength is still lower than the sintered WC-Co ball. As discussed earlier, the WC-Co ball's wear was predominantly caused by the formation of the WO<sub>x</sub> tribofilm. Some contribution of wear from the asperities of alumina coating and debris also resulted in ball wear (Fig. 8e). This can be understood from the wear rate results of APS and APS-HIP coatings, where the extent of WO<sub>x</sub> film is lower compared to the HVOF coatings; however, the ball wear is relatively higher (Table 5).

#### *Coefficient of Friction (CoF)*

Except for S-HVOF coating, the CoF initially increases during sliding wear tests, which is attributed to the absence of the W-rich tribofilm during the initial stages of the test (Fig. 8a). S-HVOF coating initially shows the lowest friction coefficient, probably due to the finer microstructure. During the steady-state period, HVOF coatings, having the highest concentration of W-rich tribofilm (Fig. 9), showed the lowest CoF. Therefore, a stable and thick tribofilm helped reduce the CoF for the HVOF and HVOF-HIP coatings. Although there was evidence of tribofilm formation in APS and APS-HIP coatings, the film was not as stable because of the coating material's fracture and delamination. The three-body wear mechanism due to entrapped debris in the APS coating wear track was also not conducive to tribofilm regeneration. The averaged steady-state CoF values shown in Fig. 8 also indicate that HIPing post-treatment had no significant effect on the steady-state friction measurement. In the case of S-HVOF coatings, the steady-state CoF value was higher than the APS and HVOF coatings. This is attributed to the relatively thin tribofilm formation in the case of S-HVOF coatings, as shown in the EDS plot and SEM observations in Fig. 9c. The wear resistance of the S-HVOF coating was the highest, which indicates that the tribofilm protected the coating; however, its thickness and stability did not facilitate a reduction in the CoF. Values of CoF are dependent upon the energy dissipation mechanism within the contact region, which relies on the tribomechanical properties of both the coating and counterbody material. The CoF values

indicated in Table 1 vary from 0.1 to 0.9 for different test couples. Although none of the previously published studies summarize in Table 1 reported the CoF in the reciprocating motion test configuration, the values reported in this investigation are in the median range of CoF.

## Conclusion

Alumina coatings prepared by APS, HVOF and S-HVOF were investigated in this study. Dry reciprocating sliding wear tests were conducted against a WC-Co ball according to the ASTM G133-02. Ground coatings were tested in the as-sprayed and post-treated HIPed conditions. The main findings of the study are as follows:

1. The APS coatings showed a significantly higher  $\alpha \rightarrow \gamma$  phase transformation during the deposition than the HVOF and S-HVOF coatings. The APS coating has poor intersplat cohesion and increased porosity. The HVOF coating used in this study exhibited a much higher content of  $\alpha$ -Al<sub>2</sub>O<sub>3</sub> than other HVOF sprayed coatings described in the literature. S- HVOF coatings showed a homogenous and dense microstructure with high  $\alpha$ -Al<sub>2</sub>O<sub>3</sub> content, corresponding to an earlier study (Ref 70).
2. A HIP treatment at 910 °C, for 2 h resulted in a decrease of the  $\alpha$ -Al<sub>2</sub>O<sub>3</sub> content in all treated coatings. The crystallization of the amorphous phase in the as-sprayed coating was attributed to this behavior.
3. After the HIP-treatment at 910 °C, significant amounts of  $\theta$ - Al<sub>2</sub>O<sub>3</sub> were found in HVOF and S-HVOF coatings. It was observed that this transition phase appeared under HIPed conditions at lower temperatures than described in the literature.
4. HIPing accompanied by nucleation and crystal growth from the amorphous phase, along with phase transformations, resulted in the cracking of HVOF and S-HVOF coatings due to residual stresses. The APS coating did not show significant cracking due to the accommodation of stress relaxation at pores and weak interlamellar bonding.
5. HVOF and S-HVOF coatings showed an order of magnitude higher sliding wear resistance (Fig. 8 and Table 5) when compared to the conventional APS coating. This performance improvement is attributed to the finer and denser coating microstructures, high  $\alpha$ -Al<sub>2</sub>O<sub>3</sub> content and high mechanical strength.
6. The wear mechanism was dominated by the formation and removal of W(Ox)-rich tribofilm and the coating fracture and entrapment of debris in the wear track. The formation and stability of this tribofilm improved the wear resistance of HVOF coatings.
7. The steady-state CoF was the highest for the S-HVOF coatings and lowest for the HVOF coatings. This is attributed to the stability of the W-rich tribofilm in the case of HVOF coatings.
8. There was no improvement in the wear resistance or CoF of the test couples after the HIPing post-treatment.
9. Improving the sliding wear resistance of alumina coatings requires further research. The current research indicates that factors such as powder size, spray process, coating parameters, and sliding wear test conditions can significantly influence variations in the wear results (Table 1) than by changing the composition to binary systems such as Al<sub>2</sub>O<sub>3</sub>-TiO<sub>2</sub>.

**Acknowledgments** The authors would like to acknowledge the ENGIN-X beam time award at the STFC ISIS Facility (experiment number RB810413) for the neutron diffraction measurements used here for comparative analysis. Thanks to Dr T. Itsukaichi, Dr J. Kitamura and Dr S. Osawa, Thermal Spray Materials Department, Fujimi Incorporated, Japan, for thermal spraying the APS and HVOF ( $\theta$ -gun) specimens. The authors are grateful to Dr Edreese Alsharaeh at Alfaisal University, KSA, for the nanoindentation measurements of HIPed samples and Mr Vishakh Kumar at Heriot-Watt University for support with the porosity analysis, as well Kerstin Gnauck at Fraunhofer IKTS for SEM investigations.

**Author Contributions** All author contributions are acknowledged.

**Funding** Not applicable.

**Data Availability** Not applicable.

**Code Availability** Not applicable.

**Conflict of interest** None.

**Ethical Approval** Not Applicable.

**Consent to Participate** Yes, all authors have given consent to participate and publish.

**Consent for Publication** All authors have given consent for publication.

**Open Access** This article is licensed under a Creative Commons Attribution 4.0 International License, which permits use, sharing, adaptation, distribution and reproduction in any medium or format, as long as you give appropriate credit to the original author(s) and the source, provide a link to the Creative Commons licence, and indicate if changes were made. The images or other third party material in this article are included in the article's Creative Commons licence, unless indicated otherwise in a credit line to the material. If material is not included in the article's Creative Commons licence and your intended use is not permitted by statutory regulation or exceeds the permitted use, you will need to obtain permission directly from the copyright holder. To view a copy of this licence, visit <http://creativecommons.org/licenses/by/4.0/>.



## References

- E. Dörre and H. Hübner, *Alumina-Processing, Properties, and Applications*, Springer, Berlin, 1984.
- A. Ruys, *Alumina Ceramics: Biomedical and Clinical Applications*, Woodhead Publishing, New Delhi, 2019.
- R. McPherson, On the formation of thermally sprayed alumina coatings, *J. Mater. Sci.*, 1980, **15**, p 3141-3149. <https://doi.org/10.1007/BF00550387>
- P. Chráska, J. Dubsky, K. Neufuss, and J. Pisacka, Alumina-base plasma-sprayed materials part I: Phase stability of alumina and alumina-chromia, *J. Therm Spray Tech*, 1997, **6**, p 320-326. <https://doi.org/10.1007/s11666-997-0066-9>
- O. Ali, R. Ahmed, and H. Alawadhi, Sliding Wear Investigation of Plasma and High Velocity Oxy-Fuel Sprayed Alumina Coatings, *Int. Therm. Spray Conf. Expos.*, 2016, **324**, p 991-996.
- C.C. Stahr, S. Saaro, L.-M. Berger, J. Dubský, K. Neufuss, and M. Herrmann, Dependence of the stabilisation of  $\alpha$ -Alumina on the spray process, *J. Therm. Spray Technol.*, 2007, **16**, p 822-830. <https://doi.org/10.1007/s11666-007-9107-7>
- J. Dubsky, P. Chraska, B. Kolman, C.C. Stahr, and L.-M. Berger, Phase Formation Control in Plasma Sprayed Alumina-Chromia Coatings, *Ceram. Silik.*, 2011, **55**, p 294-300.
- R.J. Damani and P. Makroczy, Heat treatment induced phase and microstructural development in bulk plasma sprayed alumina, *J. Eur. Ceram. Soc.*, 2000, **20**(7), p 867-888. [https://doi.org/10.1016/S0955-2219\(99\)00217-4](https://doi.org/10.1016/S0955-2219(99)00217-4)
- L.-M. Berger, Tribology of Thermally Sprayed Coatings in the  $\text{Al}_2\text{O}_3$ - $\text{Cr}_2\text{O}_3$ - $\text{TiO}_2$  System, *Thermal Sprayed Coatings and their Tribological Performances*. M. Roy, J.P. Davim Ed., IGI Global, Hershey, 2015. <https://doi.org/10.4018/978-1-4666-7489-9.ch008>
- L.-M. Berger, F.-L. Toma, S. Scheitz, R. Trache, and T. Börner, Thermisch Gespritzte Schichten im System  $\text{Al}_2\text{O}_3$ - $\text{Cr}_2\text{O}_3$ - $\text{TiO}_2$ -ein Update, *Mater-wiss. u. Werkstofftech.*, 2014, **45**, p 465-475. <https://doi.org/10.1002/mawe.201400260>
- G. Bolelli, L. Lusvardi, T. Manfredini, F.P. Mantini, R. Polini, E. Turunen et al., Comparison Between Plasma- and HVOF-Sprayed Ceramic Coatings, *Part I: Microstruct. Mech. Prop. Int. J. Surf. Sci. Eng.*, 2007, **1**(1), p 38-61. <https://doi.org/10.1504/IJSURFSE.2007.013620>
- K. Niemi, P. Vuoristo, and T. Mäntylä, Properties of Alumina-Based Coatings Deposited by Plasma Spray and Detonation Gun Spray Processes, *J. Therm. Spray Technol.*, 1994, **3**(2), p 199-203. <https://doi.org/10.1007/BF02648279>
- P. Saravanan, V. Selvarajan, D.S. Rao, S.V. Joshi, and G. Sundararajan, Influence of Process Variables on the Quality of Detonation Gun Sprayed Alumina Coatings, *Surf. Coat. Technol.*, 2000, **123**(1), p 44-54. [https://doi.org/10.1016/S0257-8972\(99\)00252-2](https://doi.org/10.1016/S0257-8972(99)00252-2)
- G. Sundararajan, K.U.M. Prasad, D.S. Rao, and S.V. Joshi, A Comparative Study of Tribological Behavior of Plasma and D-Gun Sprayed Coatings under Different Wear Modes, *J. Mater. Eng. Perform.*, 1998, **7**(3), p 343-351. <https://doi.org/10.1361/105994998770347783>
- I. Shakhova, E. Mironov, F. Azarmi, and A. Safonov, Thermo-Electrical Properties of the Alumina Coatings Deposited by Different Thermal Spraying Technologies, *Ceram. Int.*, 2017, **43**, p 15392-15401. <https://doi.org/10.1016/j.ceramint.2017.08.080>
- F.-L. Toma, A. Potthoff, L.-M. Berger, and C. Leyens, Demands, Potentials, and Economic Aspects of Thermal Spraying with Suspensions: A Critical Review, *J. Therm. Spray Technol.*, 2015, **24**(7), p 1143-1152. <https://doi.org/10.1007/s11666-015-0274-7>
- M. Hauer, M. Meyer, D. Billieres, C. Bricquet, F. Gerstgrasser, J. Kiilakoski, J. Lejay, and K.-M. Henkel, Use of Different Process Gases for Manufacturing Isolating Alumina Coatings by Flame Spraying with Cords, *J. Therm. Spray Technol.*, 2021, **30**, p 222-235. <https://doi.org/10.1007/s11666-021-01160-8>
- T.A. Owoseni, J.W. Murray, Z. Pala, E.H. Lester, D.M. Grant, and T. Hussain, Suspension High Velocity Oxy-Fuel (SHVOF) Spray of Delta-Theta Alumina Suspension: Phase Transformation and Tribology, *Surf. Coat. Technol.*, 2019, **371**, p 97-106. <https://doi.org/10.1016/j.surfcoat.2018.08.047>
- E. Turunen, T. Varis, T.E. Gustafsson, J. Keskinen, T. Fält, and S.-P. Hannula, Parameter Optimisation of HVOF Sprayed Nanostructured Alumina and Alumina-nickel Composite Coatings, *Surf. Coat. Technol.*, 2006, **200**(16-17), p 4987-4994. <https://doi.org/10.1016/j.surfcoat.2005.05.018>
- F.-L. Toma, S. Scheitz, L.-M. Berger, V. Sauchuk, M. Kusnezoff, and S. Thiele, Comparative Study of the Electrical Properties and Characteristics of Thermally Sprayed Alumina and Spinel Coatings, *J. Therm. Spray Technol.*, 2011, **20**, p 195-204. <https://doi.org/10.1007/s11666-010-9580-2>
- G.N. Heintze and S. Uematsu, Preparation and Structures of Plasma-Sprayed  $\gamma$ - and  $\alpha$ - $\text{Al}_2\text{O}_3$  Coatings, *Surf. Coat. Technol.*, 1992, **50**, p 213-222. [https://doi.org/10.1016/0257-8972\(92\)90004-T](https://doi.org/10.1016/0257-8972(92)90004-T)
- N.N. Ault, Characteristics of Refractory Oxide Coatings Produced by Flame-Spraying, *J. Am. Ceram. Soc.*, 1957, **40**, p 69-74. <https://doi.org/10.1111/j.1151-2916.1957.tb12578.x>
- R. McPherson, Formation of Metastable Phases in Flame- and Plasma-Prepared Alumina, *J. Mater. Sci.*, 1973, **8**, p 851-858. <https://doi.org/10.1007/BF02397914>
- K. Sabiruddin, J. Joardar, and P.P. Bandyopadhyay, Analysis of Phase Transformation in Plasma Sprayed Alumina Coatings Using Rietveld Refinement, *Surf. Coat. Technol.*, 2010, **204**(20), p 3248-3253. <https://doi.org/10.1016/j.surfcoat.2010.03.026>
- V.S. Thompson and O.J. Whitemore Jr., Structural Changes on Reheating Plasma-Sprayed Alumina, *Am. Ceram. Soc. Bull.*, 1968, **47**(7), p 637-641.
- J.M. Guilemany, J. Nutting, and M.J. Dougan, A Transmission Electron Microscopy Study of the Microstructures Present in Alumina Coatings Produced by Plasma Spraying, *J. Therm. Spray Technol.*, 1997, **6**(4), p 425-429. <https://doi.org/10.1007/s11666-997-0025-5>
- M. Vippola, S. Ahmaniemi, J. Keränen, P. Vuoristo, T. Lepistö, T. Mäntylä, and E. Olsson, Aluminum Phosphate Sealed Alumina Coating: Characterisation of Microstructure, *Mater. Sci. Eng., A*, 2002, **323**(1), p 1-8. [https://doi.org/10.1016/S0921-5093\(01\)01367-3](https://doi.org/10.1016/S0921-5093(01)01367-3)
- M.L. Gualtieri, M. Prudenziati, and A.F. Gualtieri, Quantitative Determination of the Amorphous Phase in Plasma Sprayed Alumina Coatings Using the Rietveld Method, *Surf. Coat. Technol.*, 2006, **201**(6), p 2984-2989. <https://doi.org/10.1016/j.surfcoat.2006.06.009>
- D.I. Pantelis, P. Psyllaki, and N. Alexopoulos, Tribological Behaviour of Plasma-Sprayed Coatings Under Severe Wear Conditions, *Wear*, 2000, **237**(2), p 197-204. [https://doi.org/10.1016/S0043-1648\(99\)00324-5](https://doi.org/10.1016/S0043-1648(99)00324-5)
- G.J. Yang, C.X. Li, and C.J. Li, Characterisation of Nonmelted Particles and Molten Splats in Plasma-Sprayed  $\text{Al}_2\text{O}_3$  Coatings by a Combination of Scanning Electron Microscopy, x-ray Diffraction Analysis, and Confocal Raman Analysis, *J. Therm. Spray Technol.*, 2013, **22**(2), p 131-137. <https://doi.org/10.1007/s11666-012-9863-x>
- P. Junge, M. Greinacher, D. Kober, P. Stargardt, and C. Rupprecht, Metastable Phase Formation, *Microstruct. Dielect. Prop. Plasma-Sprayed Alum. Ceram. Coat. Coat.*, 2022, **12**, p 1847. <https://doi.org/10.3390/coatings12121847>
- E.R. Yang, X.T. Luo, G.J. Yang, C.J. Li, M. Takahashi, S. Kuroda, and K.H. Kim, Impact of Deposition Temperature on Crystalline Structure of Plasma-Sprayed  $\text{Al}_2\text{O}_3$  Splats Revealed

- by FIB-HRTEM Technique, *Ceram. Int.*, 2016, **42**(1A), p 853-860. <https://doi.org/10.1016/j.ceramint.2015.09.010>
33. I. Levin and D. Brandon, Metastable Alumina Polymorphs: Crystal Structures and Transition Sequences, *J. Am. Ceram. Soc.*, 1998, **81**, p 1995-2012.
  34. M. Herrmann, F.-L. Toma, L.-M. Berger, G. Kaiser, and C.C. Stahr, Comparative Study of the Corrosion Resistance of Thermally Sprayed Ceramic Coatings and their Bulk Ceramic Counterparts, *J. Eur. Ceram. Soc.*, 2014, **34**, p 493-504. <https://doi.org/10.1016/j.jeurceramsoc.2013.08.033>
  35. K.S. Caruso, D.G. Drewry, D.E. King, and J.S. Jones, Heat Treatment of Plasma-Sprayed Alumina: Evolution of Microstructure and Optical Properties, *Ceram Eng Sci Proc*, 2007, **28**(3), p 177-192. <https://doi.org/10.1002/9780470339510.ch18>
  36. S. Matthews, F. Taliana, and B. James, Heat Treatment of Plasma-Sprayed Al<sub>2</sub>O<sub>3</sub> and Al<sub>2</sub>O<sub>3</sub>-WO<sub>3</sub> coatings between 500 and 1000 °C, *Surf. Coat. Technol.*, 2012, **212**, p 109-118. <https://doi.org/10.1016/j.surfcoat.2012.09.030>
  37. G. Bolelli, V. Cannillo, R. Gadow, A. Killinger, L. Lusvardi, T. Manfredini, P. Müller, and P., Properties of Al<sub>2</sub>O<sub>3</sub> coatings by High Velocity Suspension Flame Spraying (HVSFS): Effects of Injection Systems and Torch Design, *Surf. Coat. Technol.*, 2015, **270**, p 175-189. <https://doi.org/10.1016/j.surfcoat.2015.03.005>
  38. R.J. Damani and P. Makroczy, Heat Treatment Induced Phase and Microstructural Development in Bulk Plasma Sprayed Alumina, *J. Eur. Ceram. Soc.*, 2000, **20**(7), p 867-888. [https://doi.org/10.1016/S0955-2219\(99\)00217-4](https://doi.org/10.1016/S0955-2219(99)00217-4)
  39. M. Rudolph, M. Motylenko, and D. Rafaja, Structure Model of  $\gamma$ -Al<sub>2</sub>O<sub>3</sub> Based on Planar Defects, *IUCrJ*, 2019, **6**(Pt 1), p 116-127. <https://doi.org/10.1107/S2052252518015786>
  40. L. Kovarik, M. Bowden, A. Genc, J. Szanyi, C.H.F. Peden, and J.H. Kwak, Structure of  $\delta$ -Alumina: Toward the Atomic Level Understanding of Transition Alumina Phases, *J. Phys. Chem. C*, 2014, **118**, p 18051-18058. <https://doi.org/10.1021/jp500051j>
  41. L. Kovarik, M. Bowden, A. Andersen, N.R. Jaegers, N. Washton, and J. Szanyi, Quantification of High-Temperature Transition Al<sub>2</sub>O<sub>3</sub> and Their Phase Transformations, *Chem. Int. Ed.*, 2020, **59**, p 21719-21727. <https://doi.org/10.1002/anie.202009520>
  42. L. Li, B. Kharas, H. Zhang, and S. Sampath, Suppression of Crystallisation During High Velocity Impact Quenching of Alumina Droplets: Observations and Characterisation, *Mater. Sci. Eng. A*, 2007, **456**(1-2), p 35-42. <https://doi.org/10.1016/j.msea.2006.11.132>
  43. G. Sivakumar, R.O. Dusane, and S.V. Joshi, A Novel Approach to Process Phase Pure  $\alpha$ -Al<sub>2</sub>O<sub>3</sub> Coatings by Solution Precursor Plasma Spraying, *J. Eur. Ceram. Soc.*, 2013, **33**, p 2823-2829. <https://doi.org/10.1016/j.jeurceramsoc.2013.05.005>
  44. G. Sivakumar, M. Ramakrishna, R.O. Dusane, and S.V. Joshi, Effect of SPPS Process Parameters on In-Flight Particle Generation and Splat Formation to Achieve Pure  $\alpha$ -Al<sub>2</sub>O<sub>3</sub> Coatings, *J. Therm. Spray Technol.*, 2015, **24**, p 1221-1234. <https://doi.org/10.1007/s11666-015-0284-5>
  45. H. Shun, C.-J. Li, and G.-J. Yang, Influence of Deposition Temperature on the Microstructures and Properties of Plasma-Sprayed Al<sub>2</sub>O<sub>3</sub> Coatings, *J. Therm. Spray Technol.*, 2011, **20**(1-2), p 160-169. <https://doi.org/10.1007/s11666-010-9591-z>
  46. F.-L. Toma, L.-M. Berger, C.C. Stahr, T. Naumann, S. Langner, DE 10 2008 026 101 B4, filed: 30.5.2008, granted: 18.2.2010; EP 2300630 A1; WO 2009/146832 A1; US 8,318,261, B2; CA 2726434 A1; JP 2011- 522115 A.
  47. M. Michalak, L. Latka, P. Sokolowski, F.-L. Toma, H. Myalska, A. Denoirjean, and H. Ageorges, Microstructural, mechanical and tribological properties of finely grained Al<sub>2</sub>O<sub>3</sub> coatings obtained by SPS and S-HVOF methods, *Surf. Coat. Technol.*, 2020, **404**, p 126463-126478. <https://doi.org/10.1016/j.surfcoat.2020.126463>
  48. M. Grimm, S. Conze, L.-M. Berger, R. Drehmann, and T. Lampke, Microstructure and Properties of Atmospheric Plasma Sprayed (Al, Cr)<sub>2</sub>O<sub>3</sub>-TiO<sub>2</sub> Coatings from Blends, *J. Therm. Spray Technol.*, 2022, **31**, p 256-268. <https://doi.org/10.1007/s11666-021-01289-6>
  49. M. Nowakowska, L. Latka, P. Sokolowski, M. Szala, F.-L. Toma, and M. Walczak, Investigation into microstructure and mechanical properties effects on sliding wear and cavitation erosion of Al<sub>2</sub>O<sub>3</sub>- TiO<sub>2</sub> coatings sprayed by APS SPS and S-HVOF, *Wear*, 2022, **508-50**, p 204462. <https://doi.org/10.1016/j.wear.2022.204462>
  50. G. Bolelli, L. Lusvardi, T. Manfredini, F. Pighetti Mantini, E. Turunen, T. Varis, and S.-P. Hannula, Comparison Between Plasma- and HVOF-Sprayed Ceramic Coatings Part II: Tribological Behaviour, *Int. J. Surf. Sci. Eng.*, 2007, **1**(1), p 62-79. <https://doi.org/10.1504/IJSURFSE.2007.013621>
  51. N.H. Faisal and R. Ahmed, Acoustic Emission Analysis of Vickers Indentation Fracture of Cermet and Ceramic Coatings, *Meas. Sci. Technol.*, 2011, **22**(12), p 125704.
  52. R. Ahmed, N.H. Faisal, A.M. Paradowska, and M.E. Fitzpatrick, Residual Strain and Fracture Response of Al<sub>2</sub>O<sub>3</sub> Coatings Deposited via APS and HVOF Techniques, *J. Therm. Spray Technol.*, 2012, **21**(1), p 23-40.
  53. N.H. Faisal, R. Ahmed, A.K. Prathuru, S. Spence, M. Hossain, and J.A. Steel, An Improved Vickers Indentation Fracture Toughness Model to Assess the Quality of Thermally Sprayed Coatings, *Eng. Fract. Mech.*, 2014, **128**, p 189-204.
  54. S.M. Ang and C.C. Berndt, A Review of Testing Methods for Thermal Spray Coatings, *Int. Mater. Rev.*, 2014, **59**(4), p 179-223. <https://doi.org/10.1179/1743280414Y.0000000029>
  55. S. Goel, S. Björklund, N. Curry, U. Wiklund, and S. Joshi, Axial Suspension Plasma Spraying of Al<sub>2</sub>O<sub>3</sub> Coatings for Superior Tribological Properties, *Surf. Coat. Technol.*, 2017, **315**, p 80-87. <https://doi.org/10.1016/j.surfcoat.2017.02.025>
  56. T. Tesar, R. Musalek, J. Medricky, J. Kotlan, F. Lukac, Z. Pala, P. Cibor, T. Chraska, S. Houdkova, V. Rimal, and N. Curry, Development of Suspension Plasma Sprayed Alumina Coatings with High Enthalpy Plasma Torch, *Surf. Coat. Technol.*, 2017, **325**, p 277-288. <https://doi.org/10.1016/j.surfcoat.2017.06.039>
  57. J.W. Murray, A.S.M. Ang, Z. Pala, E.C. Shaw, and T. Hussain, Suspension High Velocity Oxy-Fuel (S-HVOF)-Sprayed Alumina Coatings: Microstructure, Nanoindentation and Wear, *J. Therm. Spray Technol.*, 2016, **25**, p 1700-1710.
  58. A. Khosravifard, E. Salahinejad, A.H. Yaghtin, A. Araghi, and A. Akhbarizadeh, Tribochemical Behavior of Alumina Coatings Deposited by High-Velocity Oxy Fuel Spraying, *Ceram. Int.*, 2015, **41**, p 5713-5720.
  59. S.T. Aruna and N. Balaji, Influence of Critical Parameters on the Properties of Plasma Sprayed Coatings Prepared from Spray Dried Alumina Powder, *Trans. Indian Ceram. Soc.*, 2014, **73**, p 293-298.
  60. P.A. Manojkumar, A.S. Gandhi, M. Kamaraj, and A.K. Tyagi, Sliding Wear Behaviour of Alumina Coatings Prepared from Mechanically Milled Powders, *Wear*, 2014, **313**, p 11-18.
  61. V.P. Singh, A. Sil, and R. Jayaganthan, A Study on Sliding, and Erosive wear Behavior of Atmospheric Plasma Sprayed Conventional and Nanostructured Alumina Coatings, *Mater. Des.*, 2011, **32**, p 584-591.
  62. O. Tingaud, P. Bertrand, and G. Bertrand, Microstructure and Tribological Behavior of Suspension Plasma Sprayed Al<sub>2</sub>O<sub>3</sub> and Al<sub>2</sub>O<sub>3</sub>-YSZ Composite Coatings, *Surf. Coat. Technol.*, 2010, **205**, p 1004-1008. <https://doi.org/10.1016/j.surfcoat.2010.06.003>
  63. G. Darut, F. Ben-Ettouil, A. Denoirjean, G. Montavon, H. Ageorges, and P. Fauchais, Dry Sliding Behavior of Sub-Micrometer-Sized Suspension Sprayed Ceramic Oxide Coatings, *J. Therm. Spray Technol.*, 2010, **19**(1-2), p 275-285.

64. G. Bolelli, J. Rauch, V. Cannillo, A. Killinger, L. Lusvarghi, and R. Gadow, Microstructural and Tribological Investigation of High-Velocity Suspension Flame Sprayed (HVSFS)  $\text{Al}_2\text{O}_3$  Coatings, *J. Therm. Spray Technol.*, 2009, **18**, p 35-49. <https://doi.org/10.1007/s11666-008-9279-9>
65. G. Darut, H. Ageorges, A. Denoirjean, G. Montavon, and P. Fauchais, Effect of the Structural Scale of Plasma-Sprayed Alumina Coatings on Their Friction Coefficients, *J. Therm. Spray Technol.*, 2008, **17**, p 788-795. <https://doi.org/10.1007/s11666-008-9255-4>
66. G. Bolelli, L. Lusvarghi, T. Varis, E. Turunen, M. Leoni, P. Scardi, C.L.A. Ricardo, and M. Barletta, Residual Stresses in HVOF-Sprayed Ceramic Coatings, *Surf. Coat. Technol.*, 2008, **202**, p 4810-4819. <https://doi.org/10.1016/j.surfcoat.2008.04.066>
67. G. Bolelli, V. Cannillo, L. Lusvarghi, and T. Manfredini, Wear Behavior of Thermally Sprayed Ceramic Oxide Coatings, *Wear*, 2006, **261**, p 1298-1315. <https://doi.org/10.1016/j.wear.2006.03.023>
68. P.P. Psyllaki, M. Jeandin, and D.I. Pantelis, Microstructure and Wear Mechanisms of Thermal-Sprayed Alumina Coatings, *Mater. Lett.*, 2001, **47**, p 77-82.
69. G. Bolelli, B. Bonferroni, V. Cannillo, R. Gadow, A. Killinger, L. Lusvarghi, J. Rauch, and N. Stiegler, Wear Behaviour of High Velocity Suspension Flame Sprayed (HVSFS)  $\text{Al}_2\text{O}_3$  Coatings Produced Using Micron- and Nano-sized Powder Suspensions, *Surf. Coat. Technol.*, 2010, **204**, p 2657-2668. <https://doi.org/10.1016/j.surfcoat.2010.02.018>
70. F.-L. Toma, L.-M. Berger, C.C. Stahr, T. Naumann, and S. Langner, Microstructures and Functional Properties of Suspension-Sprayed  $\text{Al}_2\text{O}_3$  and  $\text{TiO}_2$  Coatings: An Overview, *J. Therm. Spray Technol.*, 2010, **19**(1-2), p 262-274. <https://doi.org/10.1007/s11666-009-9417-z>
71. F.-L. Toma, L.-M. Berger, S. Scheitz, S. Langner, C. Rodel, A. Potthoff, V. Sauchuk, and M. Kusnezoff, Comparison of the Microstructural Characteristics and Electrical Properties of Thermally Sprayed  $\text{Al}_2\text{O}_3$  Coatings from Aqueous Suspensions and Feedstock Powders, *J. Therm. Spray Technol.*, 2012, **21**(3-4), p 480-488. <https://doi.org/10.1007/s11666-012-9761-2>
72. T. Morishita, S. Osawa, T. Itsukaichi, HVOF Ceramic Coatings, Proceedings of the International Thermal Spray Conference and Exhibition ITSC 2004, 10-12 May 2004, Osaka, Japan, Proc. CD section: HVOF Processes and Materials 1, ASM International, Materials Park, OH, (2004), 1-4, (ISBN 3-87155-792-7).
73. S. Osawa, T. Morishita, High-velocity flame spray gun and spray method using the same, EP 1 407 824, European Patent, (2005).
74. J. Kitamura, H. Ibe, F. Yuasa, and H. Mizuno, Plasma Sprayed Coatings of High-Purity Ceramics for Semiconductor and Flat-Panel-Display Production Equipment, *J. Therm. Spray Technol.*, 2008, **17**(5-6), p 878-886. <https://doi.org/10.1007/s11666-008-9285-y>
75. O. Ali, R. Ahmed, N.H. Faisal, N.M. Al-Anazi, Y.O. Elakwah, and M.F.A. Goosen, Nanoindentation Evaluation of Suspension Thermal Sprayed Nanocomposite WC-Co Coatings, *Key Eng. Mater.*, 2017, **735**, p 225-229.
76. R. Ahmed, O. Ali, C.C. Berndt, and A. Fardan, Sliding Wear of Conventional and Suspension Sprayed Nanocomposite WC-Co Coatings: An Invited Review, *J. Therm. Spray Technol.*, 2021, **30**, p 800-861. <https://doi.org/10.1007/s11666-021-01185-z>
77. L.M. Gualtieri, M. Prudenziati, and A.F. Gualtieri, Quantitative Determination of the Amorphous Phase in Plasma Sprayed Alumina Coatings Using the Rietveld Method, *Surf. Coat. Technol.*, 2006, **201**(6), p 2984-2989. <https://doi.org/10.1016/j.surfcoat.2006.06.009>
78. R. Ahmed, H. Yu, L. Edwards, and J. Santisteban, Neutron Diffraction Residual Strain Measurements in Post-treated Thermal Spray Cermet Coatings, *Mater. Sci. Eng.-A*, 2008, **498**, p 191-202.
79. N.H. Faisal, R. Ahmed, A.K. Prathuru, A. Paradowska, and T.L. Lee, Measuring Residual Strain and Stress in Thermal Spray Coatings Using Neutron Diffractometers, *Exp. Mech.*, 2022, **62**, p 369-392. <https://doi.org/10.1007/s11340-021-00803-9>
80. S.C. Gill, *Residual stress in plasma sprayed deposits*, PhD Thesis, Gonville and Caius College, Cambridge University, UK, 1993.
81. N.H. Faisal, R. Ahmed, and R.L. Reuben, Indentation Testing and Its Acoustic Emission Response: Applications and Emerging Trends, *Int. Mater. Rev.*, 2011, **56**(2), p 98-142.
82. W. Deng, S.J. Li, G.L. Hou, X. Liu, X.Q. Zhao, Y.L. An, H.D. Zhou, and J.M. Chen, Comparative Study on Wear Behavior of Plasma Sprayed  $\text{Al}_2\text{O}_3$  Coatings Sliding Against Different Counterparts, *Ceram. Int.*, 2017, **43**(9), p 6976-6986. <https://doi.org/10.1016/j.ceramint.2017.02.122>
83. V. Fervel, B. Normand, H. Liao, C. Coddet, E. Beche, and R. Berjoan, Friction and Wear Mechanisms of Thermally Sprayed Ceramic and Cermet Coatings, *Surf. Coat. Technol.*, 1999, **111**(2-3), p 255-262. [https://doi.org/10.1016/S0257-8972\(98\)00822-6](https://doi.org/10.1016/S0257-8972(98)00822-6)
84. S. Guessasma, M. Bounazef, P. Nardin, and T. Sahraoui, Wear Behavior of Alumina-Titania Coatings: Analysis of Process and Parameters, *Ceram. Int.*, 2006, **32**, p 13-19.
85. L. Latka, M. Michalak, M. Szala, M. Walczak, P. Sokołowski, and A. Ambroziak, Influence of 13 wt.%  $\text{TiO}_2$  content in alumina-titania powders on microstructure, sliding wear and cavitation erosion resistance of APS sprayed coatings, *Surface and Coatings Technology*, 2021, **410**, p 126979. <https://doi.org/10.1016/j.surfcoat.2021.126979>
86. R. Ahmed, N.H. Faisal, N.M. Al-Anazi, S. Al-Mutairi, F.L. Toma, L.M. Berger, and M.F.A. Goosen, Tribo-Mechanical Evaluation of Suspension Thermal Sprayed WC-Co Nanocomposite COATINGS, *J. Therm. Spray Technol.*, 2015, **24**(3), p 357-377. <https://doi.org/10.1007/s11666-014-0174-2>
87. R. Ahmed, O. Ali, N.H. Faisal, N.M. Al-Anazi, S. Al-Mutairi, F.L. Toma, and M.F.A. Goosen, Sliding Wear Investigation of Suspension Sprayed WC-Co Nanocomposite Coatings, *Wear*, 2015, **322**, p 133-150. <https://doi.org/10.1016/j.wear.2014.10.021>
88. R. Ahmed and H.L. de Villiers Lovelock, Friction and Wear of Cobalt-Base Alloys, *Friction, Lubrication, and Wear Technology*. G.E. Totten Ed., ASM Handbook, Geauga, 2018
89. H. Engqvist, H. Högberg, G.A. Botton, S. Ederyd, and N. Axén, Tribofilm Formation on Cemented Carbides in dry Sliding Conformal Contact, *Wear*, 2000, **239**(2), p 219-228.
90. O. Ali, R. Ahmed, N.H. Faisal, N.M. Alanazi, L.-M. Berger, A. Kaiser, F.-L. Toma, E.K. Polychroniadis, M. Sall, Y.O. Elakwah, and M.F.A. Goosen, Influence of Post-Treatment on the Microstructural and Tribomechanical Properties of Suspension Thermally Sprayed WC-12 wt.% Co Nanocomposite Coatings, *Tribol. Lett.*, 2017 <https://doi.org/10.1007/s11249-017-0815-y>
91. S. Conze, L.-M. Berger, A. Richter, and R. Vaßen, Advanced Development of Coatings of the  $\text{Al}_2\text{O}_3$ - $\text{TiO}_2$  System, *Therm. Spray Bull.*, 2020, **13**, p 52-59.
92. L. Latka, A. Niemiec, M. Michalak, and P. Sokołowski, Tribological Properties of  $\text{Al}_2\text{O}_3 + \text{TiO}_2$  Coatings Manufactured by Plasma Spraying, *Tribology*, 2019, **1**, p 19-24. <https://doi.org/10.5604/01.3001.0013.1431>
93. J.E. Fernandez, R. Rodriguez, Y. Wang, and A. Rincón, Sliding Wear of a Plasma-Sprayed  $\text{Al}_2\text{O}_3$  Coating, *Wear*, 1995, **181-183**, p 417-425.

**Publisher's Note** Springer Nature remains neutral with regard to jurisdictional claims in published maps and institutional affiliations.